



RAM

● ROBOTICS
AND
MECHATRONICS

REALIZING DC ELECTRIC METAMATERIALS THROUGH FUSED DEPOSITION MODELLING

M.T. (Thijs) Hamstra

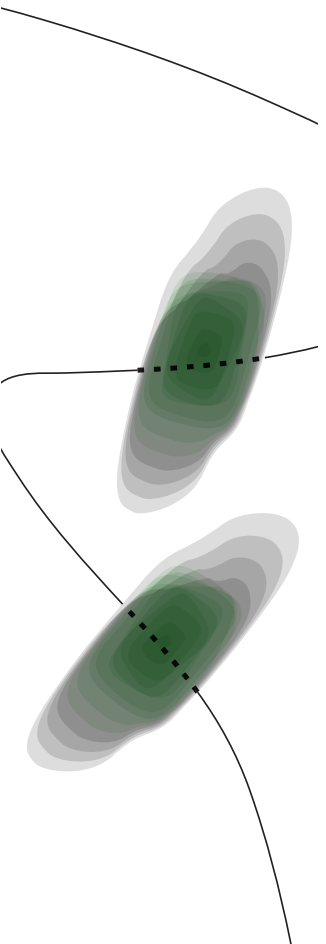
BSC ASSIGNMENT

Committee:

prof. dr. ir. G.J.M. Krijnen
ir. A.P. Dijkshoorn
prof. dr. ir. M. Odijk
dr. ir. H. Wormeester

April, 2021

020RaM2021
Robotics and Mechatronics
EEMCS
University of Twente
P.O. Box 217
7500 AE Enschede
The Netherlands



Summary

This study explores the possibility of the production of metamaterials through the Fused Deposition Modelling (FDM) process of 3D-printing. It discusses the use of anisotropic properties in conductive prints, printed with the FDM process to create sheets that are able to bend the flow of electric current. A discussion of related work shows that different properties of the printed material are important for this anisotropic conduction. This discussion ends in the derivation of an analytical model for such a metamaterial. The effect of printing parameters on the strength of the anisotropic conduction is discussed using literature and experimental results. These printing parameters include the bed and nozzle temperatures, layer height, extrusion width, extrusion multiplier and the infill density. A FEM simulation is used to determine the effect of the boundary conditions in a practical application and to test the expected effects for the extrusion width and layer height.

The metamaterials are fabricated with a consumer-grade 3D-printer on silicon wafers. Their anisotropic properties are measured using voltage probing, as the bending of current yields a skewed potential throughout the sample. The microscale structures of the printed sheets was further studied using microscopy and used to explain the observed effects. IR thermography is used to visualize the flow of current through the metamaterials.

The fabricated sheets are shown to be able to bend current to an angle 4.27° . Through studying the effects of the printing parameters used while fabricating the metamaterials, it is shown that the bed and nozzle temperatures, as well as the extrusion width, can consistently increase this angle. By combining the optimal values for these three parameters, the bending angle of the metamaterials is improved to 8.05° . A more complex metamaterial that is able to concentrate current in a certain location, known as a concentrator, is produced as a demonstration. Its conduction characteristics are visualized by IR thermography. By using the optimal parameter settings, the current concentration effect becomes visually stronger.

Contents

1	Introduction	1
1.1	Current knowledge	1
1.2	Research focus and application	1
1.3	Goals	2
1.4	Report structure	2
2	Related work and analysis	3
2.1	Anisotropy and 3D-printing	3
2.2	Thermal refraction and electric field bending	5
2.3	Conclusions	7
3	Influencing anisotropy of 3D-printed samples	8
3.1	Sintering	8
3.2	Printing temperature	8
3.3	Layer height and traxel width	10
3.4	Extrusion multiplier and infill density.	10
3.5	Conclusions	11
4	Finite Element Method Model	12
4.1	Finite Element Modelling	12
4.2	Baseline and verification	13
4.3	The effect of geometries	15
4.4	Voltage difference and bending angle	18
4.5	Conclusions	19
5	Fabrication and measurement methodology	20
5.1	Sample preparation	20
5.2	Infrared Camera	21
5.3	Probing	22
5.4	Microscopy	23
5.5	Weighing	23
5.6	Conclusions	23
6	Results	24
6.1	Baseline sample	24
6.2	Model Comparison	24
6.3	Bed temperature	25
6.4	Nozzle temperature	25

6.5	Extrusion width	26
6.6	Extrusion multiplier and infill density	27
6.7	Layer height	29
6.8	Combined parameters	31
6.9	Metamaterial application	32
6.10	Conclusions	33
7	Discussion and conclusion	35
7.1	Discussion	35
7.2	Conclusion	37
7.3	Recommendations	38
A	Derivations of the analytical model	40
A.1	Derivation by Tarkhanyan et al.	40
A.2	β for 3D-printed anisotropic materials	42
A.3	Limits of θ for β	42
A.4	Dependency of θ on φ	42
B	Effect of meanders	44
C	Modelling as anisotropic material	46
C.1	Conductivity tensor	46
C.2	COMSOL simulation	47
D	Vertical printing	48
D.1	Experimental test	48
E	Failed fabrication methods	50
E.1	Printing surface	50
E.2	Electrical Contacts	50
F	Measurements per parameter	51
	Bibliography	52

1 Introduction

Fabrication of complicated mechanical systems, for example in robotics, is often quite an expensive and arduous process. One tool that can and has been of great aid to this fabrication process is 3D-printing [1], which allows for fast prototyping and replacements of key parts in a system. As more and more parts of systems are made through a 3D-printing process, it has also become more interesting to research the 3D-printing of sensors [2, 3]. An example is to study whether it is possible to integrate them directly into structural parts [4]. If this is possible, it further enables quick and easy production and prototyping of 3D-printed systems.

An interesting opportunity for research in this field lies in the 3D-printing of metamaterials [3, 5]. A metamaterial is an artificial structure that is engineered such that it has advantageous, often uncommon, properties [5, 6]. These properties are different from those of the bulk material it consists of and typically occur due to a structure on a small scale. Examples of 3D-printed metamaterials are given by Askari et al. [5] and include materials that have optimized mechanical properties and materials used to create highly specialized antennas.

The most prevalently occurring [2, 3] method of 3D-printing is the Fused Deposition Modelling (FDM) process. The FDM process produces 3D objects by laying down a molten filament in a line-by-line manner. This process causes anisotropic properties to occur, for example in heat conduction [7] or mechanical properties [8]. If an electrically conductive filament is used, the electrical conduction of the object will also become anisotropic [3, 9]. If this property of anisotropic conduction is used for a certain application, the printed material can be considered a metamaterial.

1.1 Current knowledge

The use of anisotropic properties to create metamaterials is not a novel idea. Banduru et al. [10] showed that it was possible to make use of anisotropic properties to create metamaterials that were able to bend heat flux. This bending effect consists of heat flux flowing from one temperature terminal to another at an angle compared to the perpendicular path between parallel terminals. The steady state conduction equations are analogous [11] for heat and current conduction. Therefore, it should be considered possible to create anisotropic metamaterials that are able to conduct DC currents in a similar way. This should then pave the way for more complicated structures [6, 10].

1.2 Research focus and application

This bachelor assignment has two main focuses. Firstly, it is to understand how the knowledge from the thermal domain on steady state metamaterials translates to the electrical domain. Specifically, how the effects observed by Banduru et al. can be replicated for DC electricity in a 3D-printed metamaterial. The second focus is to develop methods to print these metamaterials. This mainly includes studying the effects of the printing parameters such that the anisotropic properties are optimized.

The knowledge gained with this bachelor assignment could then be applied in a wide variety of applications. The examples for larger, more complicated heat conducting metamaterials given by Park et al. [6] indicate that there could be many similar possibilities for creating larger and complicated DC electric metamaterials. Examples of further applications include affecting sensors that have a location-dependent sensitivity [12], conductive sheets that can be used for targeted heating [13], or EMI shielding [14]. The general knowledge on the anisotropy of 3D-printed materials and how it is affected by printing parameters can benefit any field where

conductors are 3D-printed. This includes fields such as soft robotics [15], electrochemistry [16], or the 3D-printing of electronics [17].

1.3 Goals

The main research question of this report is:

How can the anisotropic properties of 3D-printed, conductive metamaterials be used to manipulate the flow of current through these structures?

This question can be divided into the following subquestions:

- How does the previous knowledge from the thermal domain on steady state metamaterials translate to the electrical domain?
- How do the printing properties of a 3D-printed anisotropic conductive material affect its anisotropic properties?
- How can a 3D-printer be used to produce these properties and to optimize them to achieve optimal metamaterial behaviour.

1.4 Report structure

Chapter 2 Discusses related work on 3D-printing and anisotropic conductive metamaterials and leads into an analytical model that indicates what parameters are important to the anisotropic conduction in 3D-printed metamaterials. Chapter 3 discusses how these parameters could be affected through changing the printing parameters used in the fabrication process. Chapter 4 presents a Finite Element Method model which is used to simulate the effect of some of these parameters. Chapter 5 explains how these metamaterials can be produced and the methods through which they are characterized Chapter 6 presents and discusses the results of characterizing the metamaterials and how they are affected by the printing parameters. It also shows how these parameters can be combined to combine their effects on the anisotropic conduction, and how they can be used to produce a more complicated metamaterial structure. Chapter 7 provides a reflection on the results of fabricating and characterizing the metamaterials and gives a conclusion to the research by answering the research question.

2 Related work and analysis

This chapter discusses the theoretical background behind the creation of electric metamaterials. It discusses the anisotropic properties of 3D-printed materials in greater detail and explores related literature on bending of heat and DC electric fields. A model from a related paper on bending the electric field in multilayered structures is adapted for 3D-printed metamaterials.

2.1 Anisotropy and 3D-printing

2.1.1 3D printing and electrical conduction

The first 3D-printing technologies date back to the 1980s and many different methods [18, 19] exist. The most commonly used method for 3D-printing is fused deposition modeling (FDM) [18,20]. In this method, a thermoplastic filament is deposited in lines next to and on top of each other until a 3D structure is formed. A schematic of the FDM process can be seen in Figure 2.1.

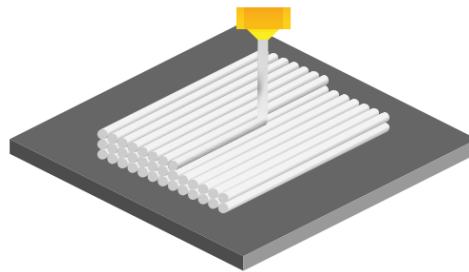


Figure 2.1: A schematic of FDM printing [20]

Conductive polymer composites exist that can be used in FDM printing to print conductive structures [3,21]. These composites consist [3] of a base printable thermoplastic that is typically either doped with carbon-based nano-particles or metal particles [22].

2.1.2 Anisotropic properties of 3D-printed conductive structures

When a material is described as anisotropic [23], it means that it has different properties along different directions. This is a property deviating from isotropy, which means the material has the same properties along each possible direction through the material. Many different types of materials [24], such as metals, ceramics and minerals, can exhibit anisotropy. One example of anisotropy is anisotropic conductivity, where a material is a better conductor of electricity in one direction than in the other.

When printed through the FDM process, 3D-printed structures show anisotropic behaviour [3]. This has been shown for example in the thermal [7] and mechanical [8, 25] domains and is thought to be caused by the line-by-line, layer-by-layer nature of the FDM process. The way the polymer molecules inside of the 3D-printed track elements (traxels) fuse with those of other lines is heavily dependent on process parameters [26] such as the layer height and nozzle temperature. Incomplete fusing of parallel traxels causes voids to appear between them, as shown in Scanning Electron Microscopy (SEM) imagery by Dijkshoorn et al., see Figure 2.2. It is thought that the anisotropy in these prints is caused by these voids and an inhomogeneous distribution of the conductive particles [27].

In conductive polymer composites, these areas of imperfect traxel fusion result in anisotropic conductivity or resistivity [3, 28]. Dijkshoorn et al. [9] analyze this anisotropy in a 3D-printed sheet of a single layer. This sheet is printed in a meandering pattern, see Figure 2.3. In analytical

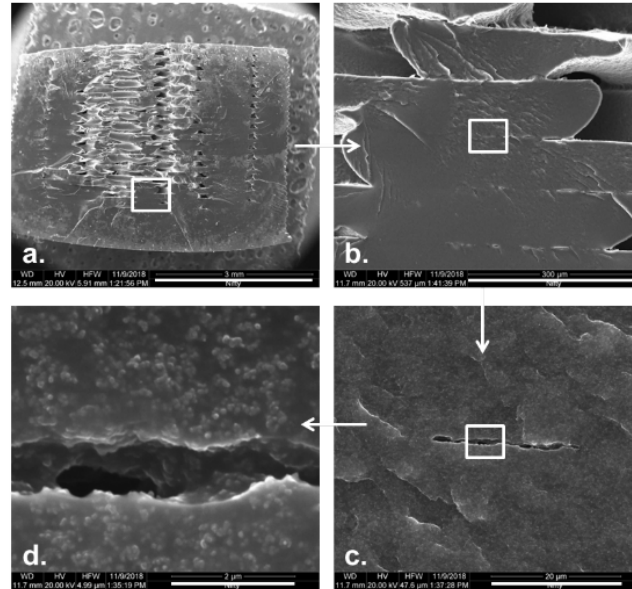


Figure 2.2: SEM images of a cross section of a 3D-printed sample, viewed from the side. Each subimage represents a zoomed-in version in the white box [27]

models, the traxels are often considered as rectangular, isotropic boxes of thickness T_w with resistivity ρ_b between which there exists a contact resistivity σ_c [9, 29].

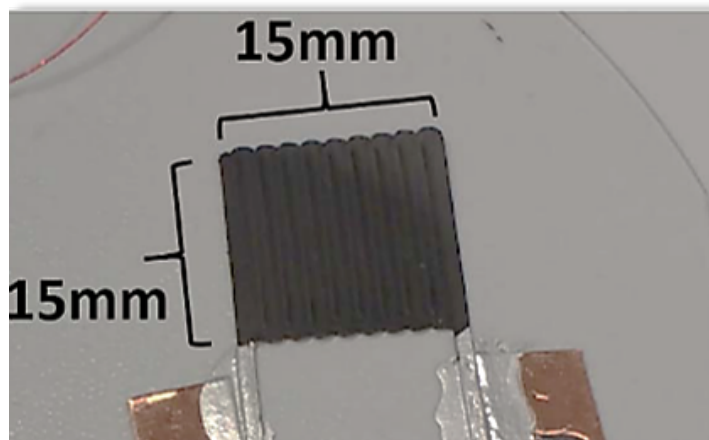


Figure 2.3: A 3D-printed conductive sheet that was characterized by Dijkshoorn et al. [9]

2.1.3 Metamaterials

Since the contact properties that arise from the FDM process give rise to additional electrical properties, sheets printed through this method can be regarded as metamaterials. Anisotropic conductive metamaterials can be used for a variety of applications [27]. In the thermal domain, metamaterials that conduct heat anisotropically have been used for bending the flow of heat [6, 10, 11]. It is thought a similar effect can be achieved through the use of 3D-printed metamaterials for bending the flow of current. The next section presents a background of related work on these effects due to anisotropy and how this knowledge applies to the 3D-printing of these metamaterials

2.2 Thermal refraction and electric field bending

2.2.1 Bending heat flux

The bending of steady state electric fields can be studied by proxy through steady-state heat conduction equations. This is because both situations are governed by equations in a similar form, the Laplace equation [11]. Steady-state heat conduction, in the absence of heat sources, is governed through Equation 2.1. In this equation, κ is the thermal conductivity and T represents the temperature.

$$\nabla \cdot (\kappa \nabla T) = 0 \quad (2.1)$$

Similarly, Equation 2.2 governs the steady state conduction of current. In this equation, σ is the electrical conductivity and V the electrical potential.

$$\nabla \cdot (\sigma \nabla V) = 0 \quad (2.2)$$

The simplest way to manipulate the direction of heat or current conduction is through using a structured sample that bends the heat flux or the electrical current from the gradient of temperature or potential. An example of this is presented in Figure 2.4 (a) where this bending is achieved through use of two dissimilar isotropic materials with different conductivities that are pressed together.

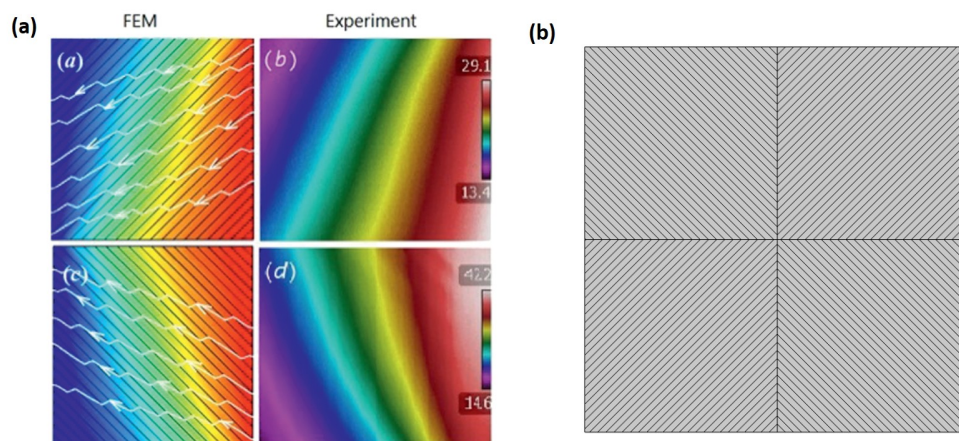


Figure 2.4: (a) Examples of diagonally oriented sheets that bend the flux of heat, including FEM simulations and experimental results [10]. (b) Design of a concentrator consisting of multiple of these sheets that is intended to concentrate heat flux or electric current in its middle.

Bandaru et al. [10] suggest that such metamaterials can then be used as building blocks for metamaterials with more complicated conduction characteristics. For example, a concentrator (see Figure 2.4 (b)) that focuses heat to a certain region, or a cloak that moves heat away from a region. Much larger examples using these building blocks to create structures with more complicated effects on heat flux, can be found in the work by Park et al. [6].

2.2.2 Bending electric fields

Tarkhanyan et al. [30] give an electrical domain analysis of a multilayer composite based on the work by Bandaru et al. In their work, they analyze a composite on which a uniform electric current density is applied. This composite consists of two isotropic conductive materials with dissimilar conductivities that are at an angle φ compared to an applied current density \vec{J}_0 . This causes the resulting electric field to be bent to an angle θ , similarly to what happens to the heat flux in Figure 2.4. A schematic can be seen in Figure 2.5.

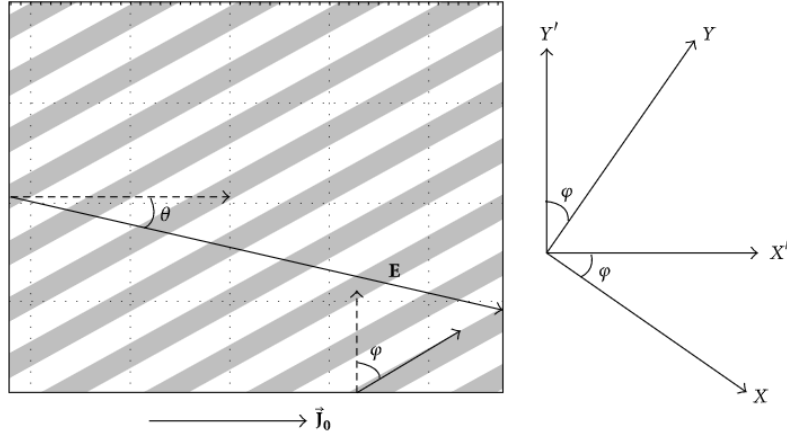


Figure 2.5: Schematic of the multilayer composite analyzed in [30]. A uniform current density \vec{J}_0 is applied to alternating layers of two materials with different isotropic conductivities at an angle φ . The resulting electric field \mathbf{E}' then is at a bending angle θ compared to the direction of the applied current density.

Their analysis of this system uses that

$$\mathbf{E} = \hat{\rho} \mathbf{J} \quad (2.3)$$

Where $\hat{\rho}$ is the resistivity tensor and \mathbf{J} is the applied current density. It is found that with an anisotropic $\hat{\rho}$ and an applied \mathbf{J} in the x -direction that θ , the angle between the applied current density and the resulting electric field is given by Equation 2.4. A derivation is given in Section A.1.

$$\tan(\theta) = \frac{E_{Y'}}{E_{X'}} = \frac{\beta \cdot \tan(\varphi)}{1 + \beta + \tan(\varphi)^2} \quad (2.4)$$

where β is a factor composed of the electrical resistivities ρ_1 and ρ_2 of both materials and their thicknesses, l_1 and l_2 respectively:

$$\beta = \frac{l_1 \cdot l_2}{(l_1 + l_2)^2} \cdot \frac{(\rho_1 - \rho_2)^2}{\rho_1 \cdot \rho_2} \quad (2.5)$$

2.2.3 Adaptation to 3D-printed objects.

For 3D-printed objects, the anisotropic conduction does not occur due to two isotropic conductive materials, but one isotropic conductive material consisting of traxels of thickness T_w with resistivity ρ_b which have a contact resistivity σ_c between them. β can be adapted to this situation by taking that $\rho_1 = \rho_b$, $l_1 = T_w$ and $l_2 \rho_2 = \sigma_c$, which assumes that the effects of the contact resistivity are homogeneous across the metamaterial. This gives the adapted β' through Equation 2.6. The derivation for β' is given in Section A.2.

$$\beta' = \lim_{l_2 \rightarrow 0, l_2 \rho_2 = \sigma_c} \beta = \frac{1}{T_w} \frac{\sigma_c}{\rho_b} \quad (2.6)$$

β' is a dimensionless factor that determines the 'strength' of the anisotropic conductivity. Therefore, it indicates the parameters that will be important to the anisotropic conductivity in the 3D-printed material. The effect of φ on θ is discussed in Section A.4.

Equation 2.6 and Equation 2.4 can not be used to predict the angle of the electric field inside the 3D-printed sample. This is because of the assumption that the effects of the contact resistivity

are homogeneous throughout the metamaterial. This assumption works for modelling the current conduction characteristics of the metamaterial, but not for modelling the behaviour of the resulting electric field. In reality, the electric field is highly concentrated in the contacts. The electric field outside of these contacts lies in the isotropic traxels and thus is parallel to the current density (see Equation 2.3). Therefore, when modelling the metamaterial as discrete traxels with boundaries, the electric field will be parallel to the current density as the 'bent' electric field lies in the infinitely thin contacts.

Even so, it is thought β' indicates that the angle of the bent current density can be influenced through at least T_w , ρ_b or σ_c . How these properties can be influenced through printing parameters is discussed in greater detail in Chapter 3. In order to study the effects of the finite geometry and different boundary conditions, an FEM model was made and is presented in Chapter 4.

2.3 Conclusions

This chapter gave an introduction to the related work in the field of FDM-induced anisotropy and the use of anisotropy to produce metamaterials. An analysis by Tarkhanyan et al. [30] was discussed and adapted to the anisotropic conduction present in 3D-printed materials. However, this analytical model can not be used as it homogenizes the properties of the infinitely thin contacts. It did show that the strength of the anisotropic conduction is determined by σ_c , ρ_b and T_w .

3 Influencing anisotropy of 3D-printed samples

In Chapter 2, it is determined that the factor β' indicates the strength of the anisotropic conduction.

$$\beta' = \frac{1}{T_w} \frac{\sigma_c}{\rho_b} \quad (3.1)$$

It is thought that ρ_b and σ_c can be affected by the printing parameters used during the fabrication process. T_w is directly related to the extrusion width, which is the width the 3D-printer tries to extrude the filament at. This chapter discusses how printing parameters can be used to influence the anisotropic conduction via these three variables.

Because there are many filaments available on the market [3], studies into printed filament properties use many different thermoplastic materials. Therefore, per filament only a small number of studies exist that investigate its properties. As a consequence, this chapter makes use of studies on a variety of filaments, assuming that the effects studied will also, to a certain extent, apply to other 3D-printing filaments.

3.1 Sintering

Sintering is the process through which layers and traxels of 3D-prints bond together [31]. It takes place above the glass transition temperature T_g of the used filament [26]. During the process, the polymers in two traxels cross over into the other traxel and bond together. This causes the neck, the contact surface between both traxels, to grow [31]. A schematical representation of this process can be seen in Figure 3.1. This causes mechanical strengthening [26,31] of the bonds. Because a weaker sintering process results in worse bonding between traxels, it is thought that the amount and thickness of voids as seen in Figure 2.2 is increased. For an electrically conductive filament, it is hypothesized that the contact resistivity σ_c is then increased.

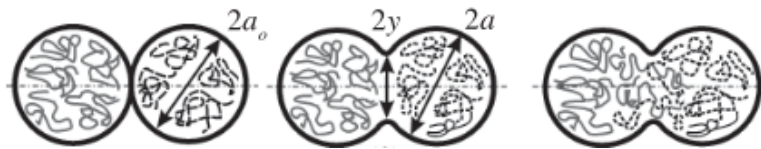


Figure 3.1: Schematic representation of the sintering process. Here, the neck is the distance $2y$. [32]

3.2 Printing temperature

3.2.1 Thermoplastic filaments

Most conductive 3D-printing filaments are based on a bulk thermoplastic material suitable for 3D-printing [3]. These materials [33] have a glass transition temperature T_g and, in the case of crystalline polymers, also a melting temperature T_m . For the Fused Deposition Modelling (FDM) process, it is important that the filament becomes liquid enough [1, 20] to be extruded without blocking the nozzle and to this end it is heated far above its T_g and sometimes even above T_m . One parameter affecting sintering and thus the contact resistivity is the temperature of the printed filament [26, 34]. There are two printing parameters that affect this temperature. These are the nozzle temperature, at which the filament is extruded from the nozzle, and the temperature of the bed that it is printed on.

3.2.2 Nozzle Temperature

In the FDM process [1, 20], the nozzle is heated in order to liquidify the filament to the point it can be extruded. This gives the filament its initial temperature. The effect of the nozzle temperature on the sintering process was studied by Bellehumeur et al. [32] for an ABS P400 filament, see Figure 3.2 (a). In this case, the comparison between extruding ABS at 260 °C and 280 °C shows that using a higher extrusion temperature improves neck growth between two lines of the filament. This indicates a lower nozzle temperature has a negative effect on the sintering process and thus might increase the contact resistivity. This would cause an increase of the bending angle. It should be noted that the research by Bellehumeur et al. [32] uses an ABS filament in a printer using a heated chamber with an enveloping temperature.

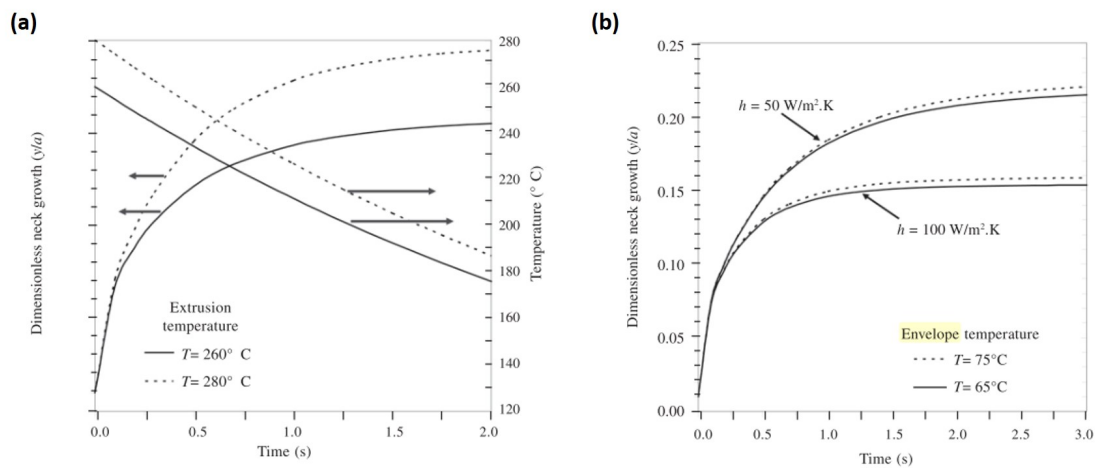


Figure 3.2: (a) Effect of extrusion temperature on dimensionless neck growth between ABS P400 traxels. The temperature on the right axis. (b) Dimensionless neck growth profiles for ABS P400 at different envelope temperatures. The envelope temperature is thought to give an indication of the effect of the bed temperature. [32]

3.2.3 Bed Temperature

The printing surface is heated [20] in order to ensure the print does not become warped and sticks well. It is thought that keeping the heated bed at a temperature above T_g of the used filament will improve sintering directly [26, 34]. If the printing bed is above ambient temperatures, it can still improve the sintering process through its temperature because higher bed temperatures will cause less heat leak from the filament into the bed, thus keeping the filament at a sintering temperature longer. This indicates that decreasing the bed temperature will likely improve sintering and thus decrease the contact impedance. Figure 3.2(b) shows the effect of keeping the extruded filament in different enveloping temperatures. It is hypothesized that the bed temperature dependence will show similar effects as the enveloping temperature. In this case, the envelope temperature was shown to have a small effect on the neck growth.

3.2.4 Effect on bulk properties

It is thought that the temperature the filament is printed at might also have an effect on its bulk resistivity. Palmic et al. [22] showed that the resistivity of Electrify conductive filament had a minimal value at a single nozzle temperature. They assumed that these differences were caused by imperfections such as cracks in the printed filament, which occurred more at certain temperatures. However, the used filament was conductive through doping with metallic nanoparticles and not carbon-based particles.

3.2.5 Ironing

Ironing is a post-treatment method whereby the heated nozzle is moved over the surface of the print without printing. Ironing has been shown [35] to reduce the surface roughness of printed objects. Therefore, there is a chance it might affect the contact and bulk resistances of conductive filament. It is thought that ironing will decrease the anisotropic properties as providing more heat to the sample will likely decrease the contact resistance by reducing the surface roughness.

3.2.6 Fan

Most 3D-printers come fitted with fans that cool certain parts [36]. These fans prevent the parts from overheating and can allow for more exact control of the temperature. Specifically, a layer fan cools the filament coming out of the nozzle in order to solidify it more quickly, which can be vital when printing with for example PLA [37]. The speed of this fan can be controlled. It is hypothesized that the fan could have an influence on the initial temperature of the filament in the sintering process, and could therefore affect the resistivity in the contacts.

3.3 Layer height and traxel width

The layer height and traxel width (extrusion width) can influence the sample in two different ways. Both have been shown [22, 26, 28, 38] to influence the bulk resistivity as well as the contacts between the traxels for multiple filaments. However, both are also important to the geometry of the sample. It is assumed that these direct geometrical effects will be larger than the effect on the resistivities in the sample.

3.3.1 Traxel Width

The traxel width is included in Equation 3.1 and can thus have a strong direct influence on the strength of the anisotropic conductivity. The reason for this effect is that it influences the density of contacts in the material. For example, a lower traxel width leads to more contacts and thus a higher β' . This would then lead to stronger bending properties. The effect of the traxel width is modelled using the analytical and Finite Element Method models in Chapter 4

3.3.2 Layer Height

The layer height is the height of the traxel in the z -dimension. It is thought that an increased layer height will increase the cross-sectional area of the traxels and thus decrease their resistance. However, it is unknown whether the contact area scales along. In the case the contact area does not scale along only the resistance in the traxels will be lowered, causing increased anisotropic conduction. If the contact area does scale along the contact resistance will also decrease. In this case, the layer height would not affect the anisotropic conduction, but it would lower the total resistance of the sample. Figure 3.3 shows a schematic for both scenarios. It is expected that the true behaviour will likely lie between both cases, namely that the contact height will grow along at a slower rate with the layer height. Both cases are investigated in Chapter 4 through FEM simulations.

3.4 Extrusion multiplier and infill density.

The flow rate of the filament is automatically calculated by the slicing software based on the traxel width and layer height [20]. This flow rate can then be multiplied by a constant factor in order to change the amount of filament that is extruded over the course of the print. This factor is known as the extrusion multiplier [39] and it allows for manual over- or underextrusion [20] of filament out of the nozzle. It is thought that over- and under-extrusion could lead to relatively better or worse filling of voids between traxels. However, the extrusion multiplier will also affect the amount of material in the bulk of the traxels. This will cause the height of the traxels and

thus their resistance to be affected. Therefore, it is unknown whether the extrusion multiplier will cause the anisotropic conduction to actually be affected at all.

An alternative to the extrusion multiplier is the infill density [20]. The infill density is the density of the pattern the slicing software uses to fill the 3D-model of the desired print. Decreasing this infill density causes less infill to be printed in the same space, thereby increasing the space between traxels. This could affect the contact resistivity in a similar manner to the extrusion multiplier. The difference between these two parameters is that the infill density will likely not affect the amount of material in the traxels, and thus might show more effect. The infill density has previously been shown to have an effect on the electrical properties of strain sensors [40].

Incidentally, the extrusion multiplier and infill density are thought to be the easiest methods to create a sample that has a maximal bending angle. They can be used to make prints where traxels are printed but no contacts are formed. This would cause the sample to have a very high contact impedance and thus a maximal bending angle. However, the printed sample would no longer be a single metamaterial but would instead have a maximal bending angle because of the mesostructure [41] it has.

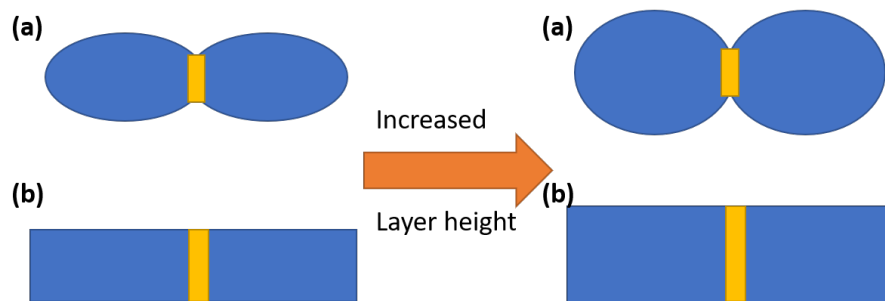


Figure 3.3: The effect of the layer height on the cross-sectional area of the traxels and the height of the contacts. (a) The height of the contacts remains constant (b) The height of the contacts is equal to the layer height

3.5 Conclusions

Table 3.1 shows the expected effects of every parameter that was tested in this research. Due to a lack of time, the effects of ironing and the layer fan were not tested experimentally.

Tested Parameter	Expected effect	FEM
Bed temperature	Effect on sintering, lower temperature increases bending and resistance	No
Nozzle temperature	Same effect as bed temperature	No
Extrusion width	Lower extrusion width means higher contact density. This would increase bending angle and resistance.	Yes
Extrusion multiplier	Lower multiplier means contacts will be of poorer quality, meaning increased bending and resistance	No
Infill density	Same effect as extrusion multiplier, but the results might have a different degree of consistency	No
Layer height	Effect on cross-sectional shape of traxels. Increased layer height is thought to decrease the bulk resistance and increase the bending angle	Yes

Table 3.1: The parameters of which the effects are experimentally tested and their expected effects.

4 Finite Element Method Model

This chapter discusses the Finite Element Method (FEM) model of the 3D-printed metamaterial. The strength of the anisotropic conduction is varied, and its effect on the angle of the current density is observed. It also shows how this model can be used to predict the effects of the extrusion width and layer height settings. A method for determining the bending angle is determined.

4.1 Finite Element Modelling

4.1.1 Model

A Finite Element Method (FEM) model is made in the COMSOL program using the Electric Currents (ec) physics module. The model consists of a 30 mm by 30 mm square. This size is chosen as it seemed of comparable magnitude to the sheets printed by Dijkshoorn et al. [9]. This square is filled with traxels at the sample angle φ . Along the boundaries of these traxels, a contact impedance σ is modelled. The left and right boundaries of the model are set to be electrically insulated, while the top boundary is considered a voltage terminal at 5 V and the bottom boundary a ground. The FEM model geometry can be seen in Figure 4.1. It should be noted that the actual samples will be fabricated in a meandering pattern, while this model does not include the meanders. Appendix B discusses the influence they have on the results of the model.

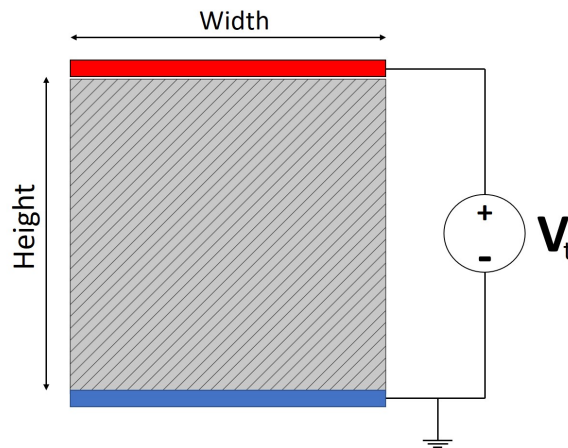


Figure 4.1: The geometry of the FEM model in COMSOL for a 45° sample angle φ . The voltage terminals are included in red and blue. The terminal voltage V_t is included as a voltage source. The blue terminal is at ground. The width and height are also defined.

When computing the results of this model, two values are considered to be of interest. These values are the resistance R of the sample, determined through a global evaluation between the terminal and ground, and the bending angle θ of the current density, determined through a point evaluation. This point evaluation is in the middle of the sample. The electric currents physics module calculates the current density vector \mathbf{J} at this point, of which the angle θ compared to the voltage terminals is determined. It should be noted that θ is not homogeneous throughout the sample, as the vertical boundaries are electrically insulated and thus force $\theta = 0^\circ$. Also note that this θ is different from that in Equation 2.4.

4.2 Baseline and verification

4.2.1 Base model

As a baseline for all simulations parameters found by Dijkshoorn et al. in [9] were used. This is because it is known that these parameters were possible and therefore realistic assumptions. The width and height that were used were based on the 15 mm by 15 mm samples made by Dijkshoorn et al. but were made twice as large to include more traxels.

ρ_b	2.8 Ωm
σ_c	$2 \times 10^{-3} \Omega\text{m}^2$
φ	45°
layer height T_{LH}	0.2 mm
traxel width T_w	0.8 mm
width W	30 mm
height H	30 mm

Table 4.1: The baseline values for the FEM model based on [9]

Using these values, a baseline simulation is computed to test the feasibility of bending the current density through making use of the anisotropic properties of 3D-printed conductive material. In Figure 4.2 the resulting current density and electric field inside of the sample is shown. The resulting angle θ in the middle of the sample is 9.03° and the resistance R of the sample is 22.2 k Ω . The found resistance is in the same order of magnitude as the sheets in the research by Dijkshoorn et al. [9].

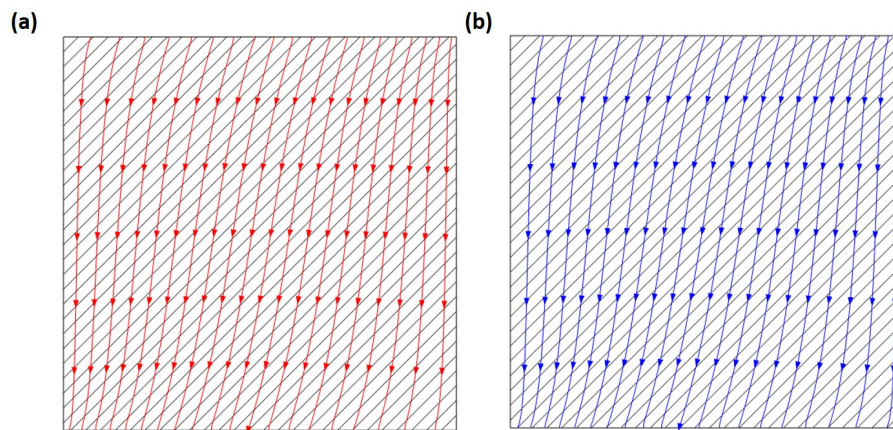


Figure 4.2: (a) Streamline of the electric current density inside the baseline sample from Figure 4.1. The positioning density of the streamlines is based on the magnitude of the current density (magnitude-controlled). (b) Magnitude-controlled streamline of the electric field.

Figure 4.2 (a) indicates that the electric current density in the baseline sample is indeed bent compared to the y -axis. Figure 4.2 (b) indicates that the electric field has the exact same streamline pattern. As mentioned in Section 2.2.3, this is because the contacts are infinitely thin which means the only electric field is that in the isotropic traxels, parallel to the electric current density.

4.2.2 Outer limits

From observation of the sample in Figure 4.1 it is clear that there are two limit cases for the current density, namely $\theta = 0^\circ$ and $\theta = 45^\circ$.

$$R = \frac{\rho \cdot L}{W \cdot H} \quad (4.1)$$

Equation 4.1 gives the resistance for a rectangle with length L , width W and height H when its resistivity ρ is known. Using this equation, the resistance for both of the outer limits can be determined. Firstly, the lower limit for R can be determined using the sample size parameters from Table 4.1 and using $\sigma_c = 0 \Omega\text{m}^2$. This gives $R = 14 \text{ k}\Omega$. The upper limit for the resistance is in the case $\lim \sigma_c \rightarrow \infty$, where conduction can only take place along the single traxel that has both a voltage terminal as well as a ground boundary. Its length is approximated to be equal to the distance from either corner of the sample. This gives $L = \sqrt{30^2 + 30^2} = 42.4 \text{ mm}$. Together with the traxel width and layer height from Table 4.1 this gives $R = 742 \text{ k}\Omega$.

To see if the model could attain the same extreme values, a parametric sweep for σ_c is performed on a logarithmic scale between $1 \times 10^{-5} \Omega\text{m}^2$ and $1 \times 10^3 \Omega\text{m}^2$ with two steps per decade. The results can be seen in Figure 4.3.

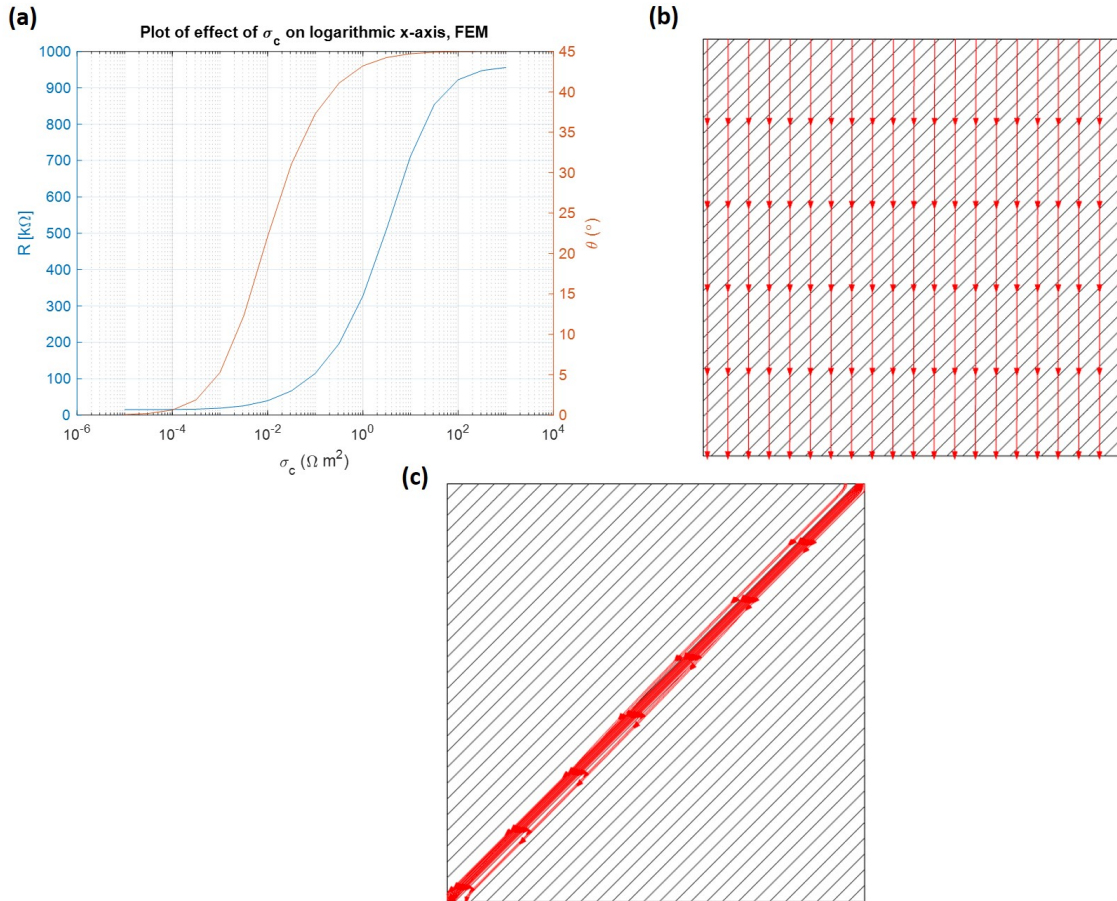


Figure 4.3: (A): The results of the logarithmic parametric sweep for σ_c . (B) The electric current density for $\sigma_c = 1 \times 10^{-5} \Omega\text{m}^2$. The field is homogeneous and perpendicular to both terminals. (C) The electric current density for $\sigma_c = 1 \times 10^3 \Omega\text{m}^2$. The current density is highly concentrated around the diagonal traxel.

It is clear from the streamline plots of the current densities that both outer situations are reached. $\sigma_c = 1 \times 10^{-5} \Omega\text{m}^2$ gave $R = 15.0 \text{ k}\Omega$ and $\theta = 0.06^\circ$ while $\sigma_c = 1 \times 10^3 \Omega\text{m}^2$ gave $R = 956 \text{ k}\Omega$ and $\theta = 45.0^\circ$. Comparing these results with the expectations shows that the limits for θ in both outer situations are almost equal to the expected values. However, there is some difference in the resistance values. The lower limit shows a difference of $1.0 \text{ k}\Omega$ with the expected value. The upper limit shows a difference of $214 \text{ k}\Omega$. The large difference in the case of the upper limit could be explained through the fact that the upper limit is calculated using an approximation of the traxel as a rectangle with the terminals connected to opposite sides, which is not actually the case.

4.2.3 Mesh convergence

In order to verify the FEM model a mesh convergence study is performed. The simulation presented in Figure 4.3 used the extremely fine physics-controlled meshing setting of COMSOL. This is the finest setting in the physics-controlled mode, and to test whether the simulation converged for increased meshing the more coarse mesh settings were also tested. The results of this mesh convergence study for the bending angle and resistance can be found in Figure 4.4

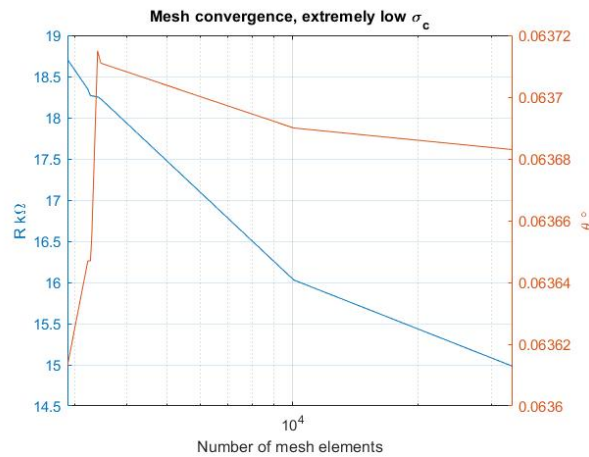


Figure 4.4: Mesh convergence study of the sample with extremely low contact resistivity. The horizontal axis data is the natural logarithm of the number of mesh elements.

The mesh convergence study used the extremely low contact resistivity value of $\sigma_c = 1 \times 10^{-5} \Omega\text{m}^2$ as for this case it is thought the sample should have $R = 14 \text{ k}\Omega$ and $\theta = 0^\circ$. As can be seen in Figure 4.4 the model does converge to roughly these values. The mesh convergence test is somewhat limited by the fact that there is a finite number of physics-controlled mesh element sizes. When a much finer, user-generated mesh is used, the resistance converges to $R = 14.6 \text{ k}\Omega$ and $\theta = 0.06^\circ$. It is thought that the small difference between these values and the theoretical ones are caused by the low yet present $\sigma_c = 1 \times 10^{-5} \Omega\text{m}^2$.

4.3 The effect of geometries

In this report, the sample length and width are considered to be codependent, such that

$$W = H \cdot \tan(\varphi) \quad (4.2)$$

which is the special case in which the diagonal is a traxel connecting the outer corners. For example, in the case $\varphi = 45^\circ$, $W = H$. The reason for this codependency is that making the sample wider or taller respectively compresses (higher bending angle) or stretches out (lower bending angle) the effect that is seen in the special case, making it sufficient to study just this special case behaviour.

This leaves four parameters in the geometry of the sample of which the effects can be studied. This includes the three geometries in the 2D-space of the sample, namely the combination of W and H , the number of traxels N and the traxel width T_w , as well as the layer height T_{LH} in the z -direction. The three geometries in 2D-space are co-dependent with two independent parameters. The effect of the layer height can be studied independently.

4.3.1 Changing traxel width

Previously, the effect of the traxel width was discussed in Section 3.3.1. There, the expectation was that the traxel width would have a strong effect on the bending angle. There is no wide consensus on the exact range of possible extrusion widths when using a certain nozzle [42, 43]. It is assumed that traxel width values of 0.30 mm up until 1.20 mm will be possible using a 0.40 mm nozzle. Therefore, this range will be used for parametric sweeps. The effect of the traxel width can be investigated in two different ways. The first method is to keep the sample size constant, which means the number of traxels in the sample is changed. The results of the parametric sweep for the traxel width in this situation can be seen in Figure 4.5.

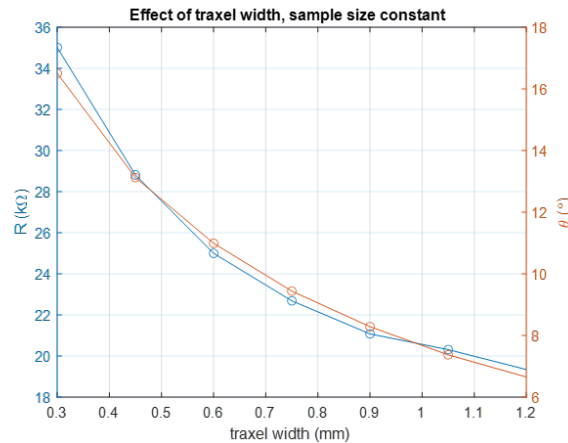


Figure 4.5: Results of the parametric sweep for traxel widths of 0.30 mm up until 1.20 mm, keeping the sample at a constant 30 mm by 30 mm.

It is clear that decreasing the traxel width in the model increases the bending angle while also increasing the resistance. This confirms the expectation presented in Section 3.3.1.

The other option is to vary the sample size to ensure that the number of traxels remains the same. This means the samples will all visually appear the same while only the scale they are on is increased. This will produce different effects, as the length of the traxels changes disproportionately compared to the length and width of the samples. As can be seen in Figure 4.6, decreasing the traxel width again results in a higher bending angle and resistance. The difference with keeping the sample size constant is the resistance, which shows slightly different behaviour compared to Figure 4.5.

4.3.2 Constant traxel width

Through keeping the traxel width constant and varying the sample size, the effect of printing larger samples with the same printer settings can be studied. This means the amount of traxels will automatically have to change to fit different sample sizes.

In Figure 4.7 (a) the results of changing the sample size while keeping the traxel width constant can be observed. The bending angle θ remains quite constant, decreasing only slightly over the course of the computations. The resistance increases without a clear mathematical relation to the size of the sample. From the previous results it can be explained that the bending angle

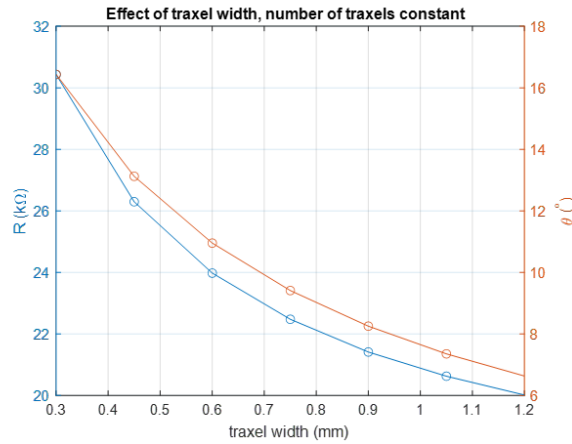


Figure 4.6: Results of the parametric sweep for traxel widths of 0.30 mm up until 1.20 mm, keeping the amount of traxels constant ($N = 54$).

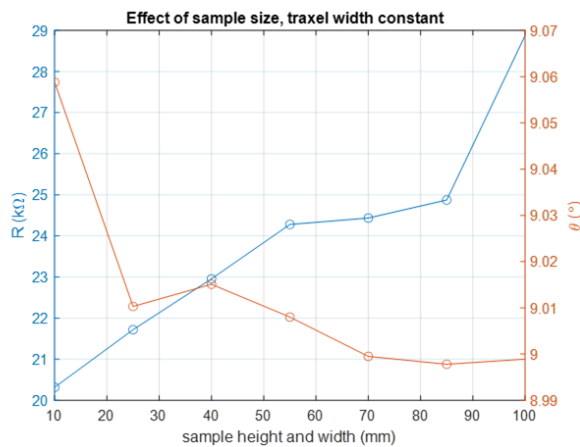


Figure 4.7: The effects of changing the sample size while keeping the traxel width constant.

remains constant. If the traxel width is first changed while keeping the number of traxels constant, the bending angle changes along inversely. If the traxel width is then changed back to its original value while the sample size is kept constant, the effect reverses and the bending angle reverses back to its original value. It should be noted, however, that this likely does not work the same for very high or very small numbers of traxels.

4.3.3 Layer height

Figure 4.8 shows the results of a parametric sweep for the layer height for both cases discussed in Section 3.3.2. This parametric sweep made use of the same model but the bulk and contact resistivities were scaled along with the changed layer height. The results confirm the expectations presented in Section 3.3.2. The resistance of the sample indeed decreases for larger layer heights. In the case the contact height does not scale along, the bending angle also increases while in the case the contact height scales along it remains constant. Therefore, it is thought that increasing the layer height will result in a decreased resistance, as well as that it could have some positive effect on the bending angle.

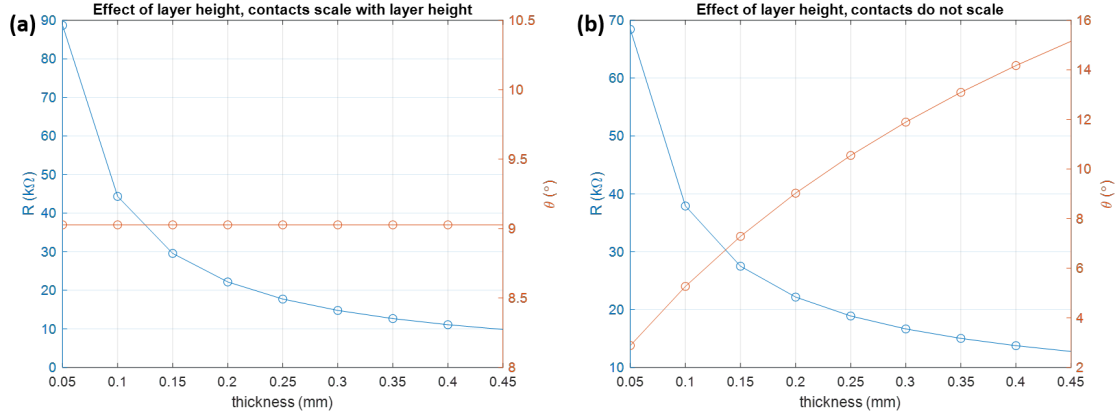


Figure 4.8: The effect of the layer height of the sample. **(a)** In the case the contacts scale along with the layer height. **(b)** In the case the contacts do not scale along with the layer height

4.4 Voltage difference and bending angle

The outer limits of the bending effect that are discussed in Section 4.2.2 inspire a method for determining the bending angle through a simple probing process. The voltage potentials of both limit cases are shown in Figure 4.9. The voltage difference between the black points in this figure will equal 0 V for a bending angle of 0° and be equal to the terminal voltage V_t for a bending angle equal to the sample angle φ . Therefore, they can be used to approximate the bending angle in the sample through linear interpolation.

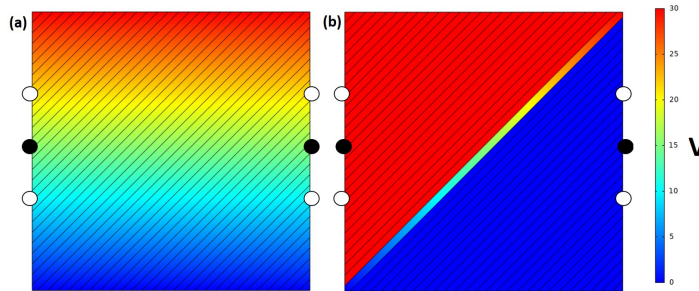


Figure 4.9: Voltage potentials for both limit cases. Black dots show the suggested probing points at $\frac{1}{2}H$, white dots show suggested probing points at $\frac{1}{3}H$ and $\frac{2}{3}H$. The color bar on the right indicates the relation between potential and voltage. **(a)** $\sigma_c = 1 \times 10^{-5} \Omega m^2$, the current density is homogeneous **(b)** $\sigma_c = 1 \times 10^5 \Omega m^2$, the current density is concentrated on the single connecting diagonal.

Figure 4.10 shows that if the voltage difference is measured at the black points in Figure 4.9, this voltage difference is very close to this linear interpolation, especially for lower θ . It also shows that measuring the average voltage difference over the two horizontals between the white points in Figure 4.9 makes the linear interpolation work even better. However, it should be noted that this method of approximating the bending angle is entirely based on observations from the FEM model. The formulas used to attain the approximate bending angle from probing the sample are:

$$V_n = \frac{\Delta V_1 + \Delta V_2}{2} \cdot \frac{1}{V_t} \quad (4.3)$$

Where:

V_n is the average normalized voltage difference

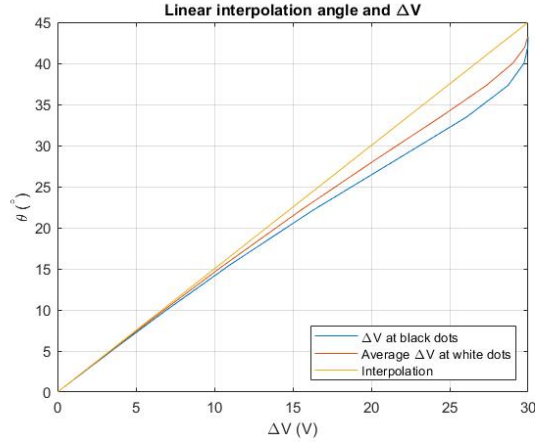


Figure 4.10: Voltage differences at different heights on the sample compared to the linear interpolation for the voltage difference between them for 0° and φ . $\varphi = 45^\circ$ and $V_t = 30\text{ V}$

ΔV_1 is the voltage difference at $\frac{1}{3}H$

ΔV_2 is the voltage difference at $\frac{2}{3}H$

Then, for the approximate bending angle θ_{app} :

$$\theta_{\text{app}} = V_n \cdot \varphi \quad (4.4)$$

4.5 Conclusions

This chapter shows that an FEM model can be used to model the flow of current through a 3D-printed metamaterial. It demonstrates the feasibility of 3D-printing metamaterials as parameters attained in previous research [9] are shown to produce a 9.03° bending angle in simulation.

There are three conclusions that can be derived from the studies on changing the geometries in the 2D geometry. Primarily, the traxel width is shown to have a large effect on the bending angle. Since it is a relatively easily changed printing parameter, this can be a good way to affect the bending properties of the sample. The second conclusion is that making larger prints with the same traxel width does not affect the bending angle. This is promising as it allows for applications that are larger in scale than the tested 30 mm by 30 mm sample. However, it should be noted this may not be the case for low numbers of traxels. The third conclusion is that the layer height could also have an effect on the bending angle, but that it is also useful for decreasing resistance in the sample.

In the case a maximal bending in a certain sample is required, it is therefore logical to choose the layer height as high as possible and the traxel width as low as possible. However, these printing parameters are limited [42, 43] by the nozzle diameter. It might prove beneficial to print the samples vertically. This will cause both of these parameters to flip around, which will increase their range of possible values in the direction that is beneficial to the bending angle. Vertical printing is further discussed in Appendix D.

Section 4.4 indicates that it is possible to approximate the bending angle through voltage probing by linearly interpolating between the two outer bending cases. However, the accuracy of this linear interpolation is entirely based on FEM simulations.

5 Fabrication and measurement methodology

This chapter discusses the fabrication of the samples and the measurement methodology that is used for analyzing the effect of the printing parameters. Appendix E discusses problems observed during the fabrication process.

5.1 Sample preparation

The process of 3D-printing starts with the creation of a .STL 3D-model of a rectangular sheet [20]. This model is then loaded into slicing software, which analyses the 3D-model and determines how it can be printed. The slicing software is the part of the fabrication process that allows for setting the previously discussed printing parameters. The slicing software generates G-code using the specified print settings, which contains the instructions for the 3D-printer.

5.1.1 Slicing

The used slicing software is PrusaSlicer. For printing the bending metamaterial, a .STL 3D-model of a rectangle is used. The rectilinear infill pattern is used as it most closely represents the FEM model seen in Figure 4.1. One downside to this pattern is that it has a meandering effect, the effect of which is further discussed in Appendix B. The meandering effect can be seen in Figure 5.1 (b).

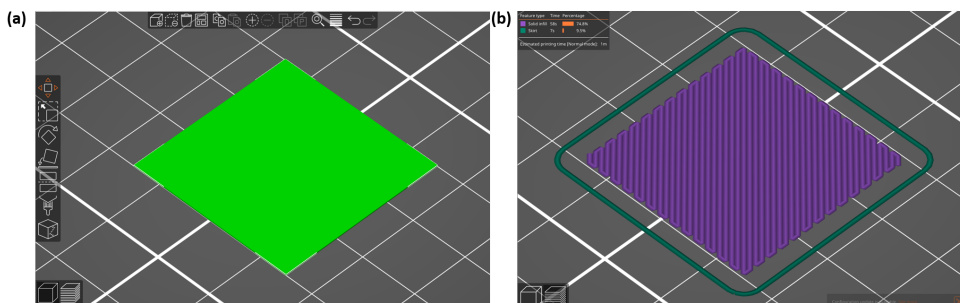


Figure 5.1: (a) The rectangular 3D-model used for printing. (b) The sliced model in which the meandering effect of the rectilinear infill pattern can be seen.

5.1.2 Printing

The sliced sample designs are printed using a consumer grade 3D printer, the Prusa MK3S. The conductive filament used in the fabrication process is the ProtoPasta Conductive PLA filament [44] because it is readily available. This filament is a compound of polylactic acid (PLA) with conductive carbon black particles. The glass transition temperature of this material is around 60 °C [45].

The printed samples have to be removable from the print bed without the removal process affecting the samples. This goal is achieved by printing on silicon wafers that are taped using temperature resistant tape to the print bed. Section E.1 provides more information on print surfaces. In order to ensure the filament sticks to the wafers, they are treated with 3D-Lac, which is a fixating spray often used for preparing glass print beds for printing. The wafers are measured to be 500 μm thick. In order to accommodate for this elevated print surface, the printer's live z -layer adjust setting is increased by 500 μm .

The baseline print parameters are given in Table 5.1. For the characterisation of their effect on the printed sample, individual parameters are changed from these default values, while the others are kept constant. A photograph of a printed sample can be seen in Figure 5.2.

Printing parameter	Value	Background
Bed temperature	50 °C	Manufacturer suggested [44]
Nozzle temperature	215 °C	Manufacturer suggested [44]
Extrusion width (traxel width)	0.6 mm	Default slicer value
Extrusion multiplier	1	Default slicer value
Infill Density	100%	Maximum, solidly fills 3D-model
Layer height (traxel thickness)	0.2 mm	Default slicer value
Nozzle diameter	0.4 mm	Only available option

Table 5.1: Default printing parameters

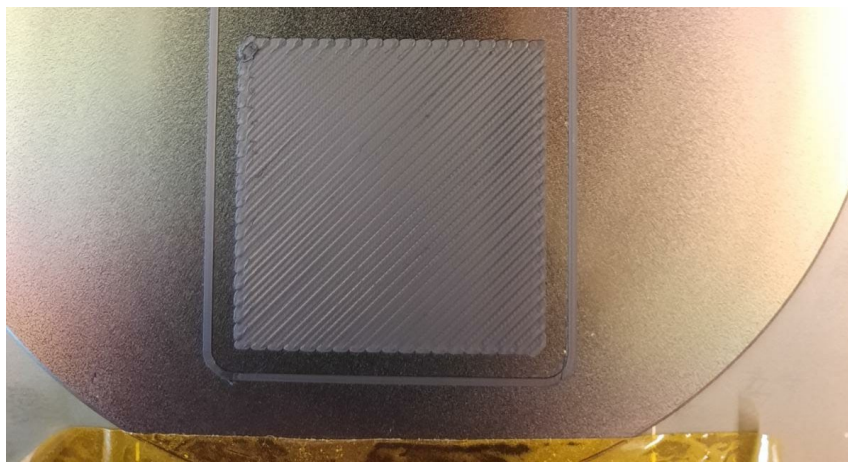


Figure 5.2: A photograph of a 3D-printed 30 by 30 mm sample printed on a silicon wafer

5.1.3 Electrical contacts

One of the biggest issues in the fabrication of these metamaterials is connecting them to electrical contacts. The contact resistance has to be equal across the entire length of the terminal or ground side of the metamaterial. The basis of the electrical contacts is 6.5 mm wide copper tape that is laid next to the side of the sample. The connection to the sample is then made using Ag-conductive paint (Electrolube SCP26G [46]). Wires are soldered to the copper tape. The other ends of these wires are attached to a voltage source using crocodile clips.

It should be noted that the Ag-conductive paint is necessary in this process due to its low viscosity because it allows for connections that completely follow the surface roughness. Issues with the electrical connections and other issues in the fabrication process are discussed in Section E.2. To block the Ag-conductive paint from flowing into the voids between the traxels, the terminal and ground sides of the sample are printed with an additional 3 layers in the z -direction. A photograph of a finished sample with electrical contacts and added layers at the terminal and ground can be seen in Figure 5.4.

5.2 Infrared Camera

In order to visualize the flow of current through the 3D-printed samples infrared thermography (IR thermography) can be used. Joule heating heats up the sample which causes it to radiate IR light. This thermal radiation can then be converted to temperature by an IR camera

(FLIR ONE Gen 2 for Android, FLIR Systems). IR thermography was considered as a method for determining the bending angle, but this proved impossible to do consistently. Therefore, IR thermography is merely used as an added tool for visualisation.

To prevent reflection from the environment affecting results, a box was made out of cardboard that could hold the IR camera and be placed around the sample, see Figure 5.3.

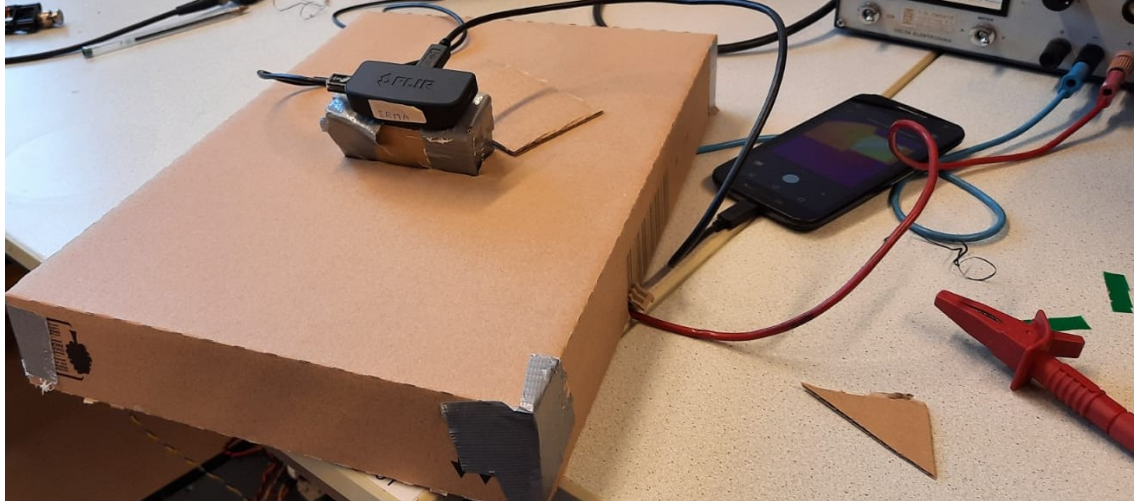


Figure 5.3: The cardboard box made to prevent heat reflection from the environment to reach the sample. The smaller box on top holds the IR camera so that only the lens is not blocked. The picture also includes the connected phone.

5.3 Probing

Another method for determining metamaterial properties is probing, used in similar research by Yang et al. [47] This method is used both for resistance and bending angle measurements. A Fluke 170 handheld digital multimeter is used for probing.

5.3.1 Resistance

Measuring the resistance of the sample is done through two-terminal probing with the digital multimeter set to the resistance setting. The probes of the multimeter are connected to the copper tapes of the electrical connections.

A four-terminal resistance measurement set-up which eliminated the resistance of the multimeter wires and the contact resistance between the probes and the copper tape showed that, together, these only accounted for 0.007 k Ω of resistance. For a typical sample, this was only around 0.7% of difference. Because of this small difference, the two-terminal set-up was used as it took significantly less time to execute. Of course, as the voltage probes were connected to the copper tape and not directly to the samples, the resistance between the copper tape and the samples was not eliminated with this process.

5.3.2 Connecting the probes

For the probing method presented in Section 4.4 the probe connections have to be consistent between samples. Probing points are added to the prints. These points are small holes designed to fit the pin of a multimeter probe. A printed sample with probing points can be seen in Figure 5.4. To get an accurate image of this voltage difference, the voltage difference at the probing points is evaluated for terminal voltages V_t of 10 V, 20 V and 30 V. The reason for using three terminal voltages is to decrease the possibility for a measurement error when measuring with just a single terminal voltage. Equation 4.3 then gives an approximation of θ .

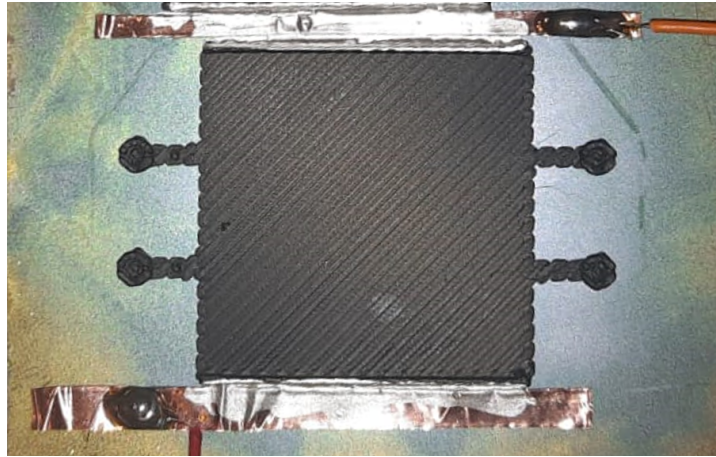


Figure 5.4: An example of a finalized sample, including four probing points and additional layers at the terminal and ground to prevent Ag-conductive paint from flowing into the contacts.

5.4 Microscopy

In order to visualize the effect of the changed printing parameters, microscopy is used. The 3D-printed samples are carefully removed from the silicon wafers. They are subsequently treated with liquid nitrogen. This cooled the samples down and allowed for them to be broken, a process called cryo-fracturing. After this, the samples are clamped and photographed by a Leica Microsystems MSV266 microscope. Both the cross-sections as well as the surfaces are photographed.

5.5 Weighing

In the cases where it was thought to give additional value to the results, some samples were removed from the silicon wafer to weigh them. Using the density of the filament [44] of 1500 kgm^{-3} and the dimensions from Table 5.1, it is determined that a typical sample will weigh around 270 mg. An Ohaus Scout Pro [48] scale was used for weighing the samples. It has a 10 mg readability.

5.6 Conclusions

This chapter shows that it is possible to produce 3D-printed metamaterials by printing them on silicon wafers treated with 3D-lac using a consumer-grade 3D printer.

6 Results

This chapter visualizes and discusses the bending properties and resistances of samples 3D-printed at 45° . The results from printing samples with default parameters are given and the FEM model is fitted to the found values. Subsequently, the results of varying each printing parameter from Table 3.1 are shown and discussed. The effect of compiling effective print parameters is shown. Finally, an example is given of a metamaterial application.

6.1 Baseline sample

The default printing parameters that produce a 'baseline' sample are presented in Table 5.1. Three samples with the baseline parameters were printed. On average, their resistance was $1.39 \text{ k}\Omega$ with a standard deviation of $0.10 \text{ k}\Omega$ while their average normalized voltage difference V_n was 0.0950 with a standard deviation of 0.003 , indicating a bending angle of 4.27° with a standard deviation of 0.15° according to the approximation from Section 4.4. The samples had an average weight of 0.26 g .

It should be noted that the number of tested samples per datapoint varies due to fabrication problems. This means that the standard deviations in the results sometimes carry a different meaning per datapoint. Appendix F includes the number of samples that was tested for each setting of each parameter. Another note is that all the graphs feature the same scale on the y-axis. This is done for easy comparison between the effects of different parameters.

6.2 Model Comparison

In Chapter 4, FEM modelling is used to predict the effect of the traxel width and the layer height. These model results can be compared to the experimental results for varying these parameters. However, the model uses the parameters from Table 4.1, which are based on results for a different filament from [27]. Thus, the model has to be adapted to the parameters for Proto-pasta conductive PLA [44]. The bulk resistivity of the material was determined by printing samples with $\varphi = 0^\circ$. The resistance in these samples was found to be $1.11 \text{ k}\Omega$ with a standard deviation of $0.06 \text{ k}\Omega$. For the volume of the samples, the layer height, width and height settings used during printing were used. The resistivity was determined to be $0.221 \text{ }\Omega\text{m}$, which is 47.5% higher than the $0.15 \text{ }\Omega\text{m}$ advertised by the manufacturer [44]. The other parameters in the model were taken from Table 5.1.

The contact resistivity was found by fitting the model to the normalized voltage difference of 0.0950 presented in Section 6.1. This method resulted in a σ_c of $4.66 \times 10^{-5} \text{ }\Omega\text{m}^2$. This contact resistivity, along with $\rho_b = 0.221 \text{ }\Omega\text{m}$ and the values in Table 5.1 were used for comparisons to the model in this chapter. The basic model has a bending angle of 4.33° and a resistance of $1.48 \text{ k}\Omega$. These values fall within the standard deviation of the results from Section 6.1. This is promising, as it indicates the approximation from Section 4.4 indeed works in this range. Table 6.1 shows the changed model parameters.

Parameter	Value
ρ_b	$0.221 \text{ }\Omega\text{m}$
σ_c	$4.66 \times 10^{-5} \text{ }\Omega\text{m}^2$
T_w	0.6 mm

Table 6.1: The changed model parameters used for comparison to experimental results. The old model parameters can be found in Table 4.1.

6.3 Bed temperature

The bed temperature was expected to have an effect on the sintering process (see Section 3.2.3). Specifically, it was expected that a lower bed temperature would have a negative effect on the contacts, thus increasing the bending angle and resistance in the samples, and that a higher bed temperature would have the opposite effect.

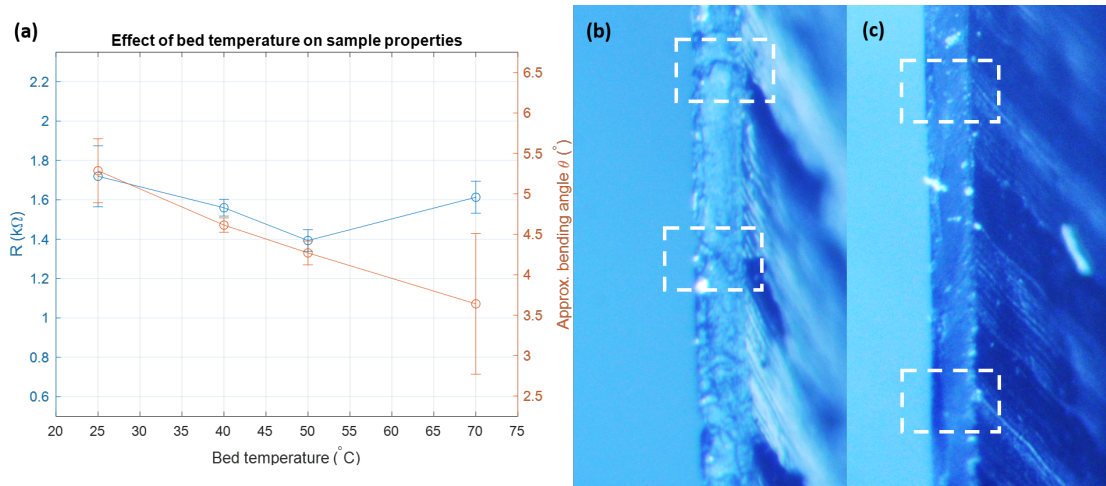


Figure 6.1: (a) Results of varying the bed temperature with errorbars of length equal to the standard deviation. (b) Microscopic view of the cross section of a sample printed at a 25 °C bed temperature. Boxes with white dashed lines indicate contacts between traxels. (c) Microscopic view of the cross section of a sample printed at a 70 °C bed temperature. Boxes with white dashed lines indicate contacts between traxels.

Figure 6.1 (a) shows that when the bed temperature is decreased from the default value of 50 °C the bending angle and resistance are increased, which is in accordance with the expectations presented in Chapter 3. The only unexpected result is that using the higher bed temperature of 70 °C results in an increased resistance. Microscopy images for two extremes of the bed temperature are shown in Figure 6.1 (b) and (c). In Figure 6.1 (b), it is shown that a lower bed temperature (25 °C) produces visible contacts in the cross-sectional microscopy view. This indicates worse sintering between the traxels. Figure 6.1 (c) shows that using a higher bed temperature (70 °C) produces no visible contacts in the cross-sectional microscopy view. This indicates improved sintering between the traxels and thus a lowered contact resistivity, which explains the decrease in bending angle.

6.4 Nozzle temperature

The nozzle temperature was also expected to have an effect on the sintering process (see Section 3.2.2). Specifically, it was thought a lower nozzle temperature would have a negative effect on the sintering, which would increase the bending angle and resistance of the sample. A higher nozzle temperature was thought to lead to the opposite effect.

Figure 6.2 (a) shows that the nozzle temperature confirms the expected effects. A lower nozzle temperature leads to an increased resistance and bending angle, while a higher nozzle temperature decreases the bending angle. Here, there is again an increased average resistance for the samples printed at a nozzle temperature of 230 °C, which, similarly to the result for a bed temperature of 70 °C, was unexpected. Figure 6.2 (b) and (c) shows microscopic images of the cross-sections of sheets printed at the outer nozzle temperatures. The effects seen here are similar to those seen in Figure 6.1 (b) and (c), as the contacts are visible for the lower tempera-

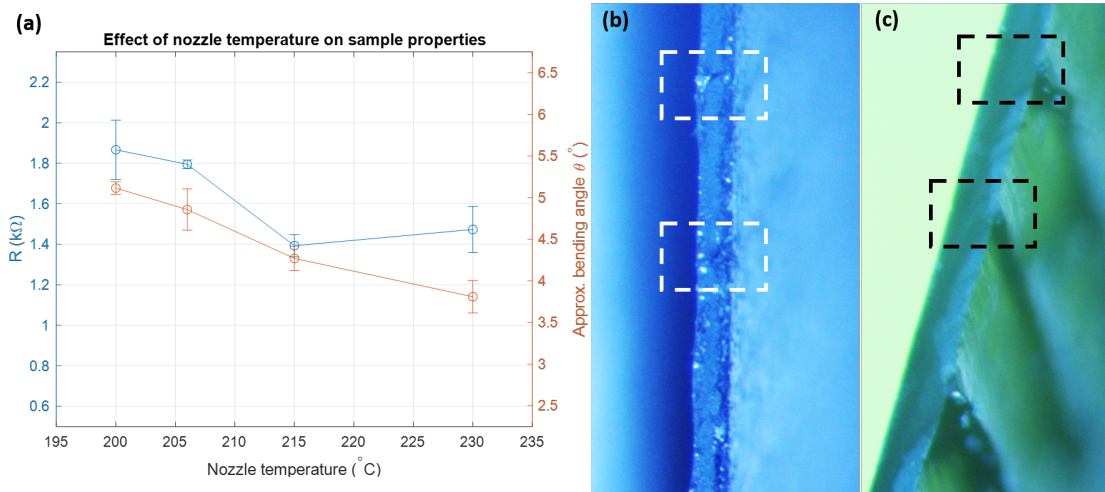


Figure 6.2: (a) Results of varying the nozzle temperature with errorbars of length equal to the standard deviation. (b) Microscopic view of the cross section of a sample printed at a 200°C nozzle temperature. Boxes with white dashed lines indicate contacts between traxels. (c) Microscopic view of the cross section of a sample printed with a 230°C nozzle temperature. Boxes with black dashed lines indicate contacts between traxels.

ture and invisible for the higher temperature. The similarity both in measurement data as well as in the microscopic images indicate that both parameters are both affect the same process.

6.5 Extrusion width

The extrusion width (traxel width) was thought to influence the properties of the sample mostly due to the effect of changing the amount of contacts in the same amount of material (see Section 3.3.1 and Section 4.3.1). This means a lower extrusion width results in more contacts and thus a larger anisotropic effect.

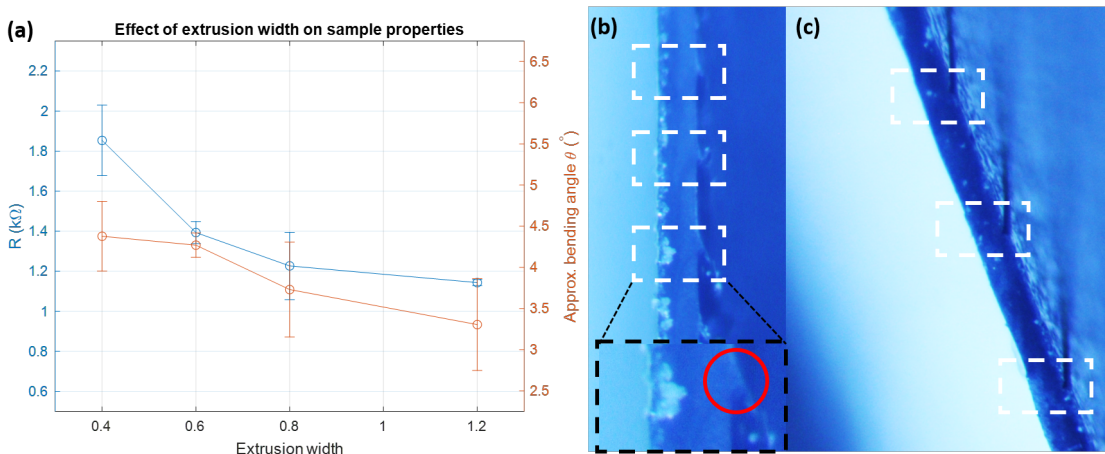


Figure 6.3: (a) Results of varying the extrusion width with errorbars of length equal to the standard deviation. (b) Microscopic view of the cross section of a sample printed with a 0.4 mm extrusion width. Boxes with white dashed lines indicate contacts between traxels. A zoomed-in view in the black box shows a red circle around an example of the ridge-like effect between the traxels. (c) Microscopic view of the cross section of a sample printed with a 1.2 mm extrusion width. Boxes with white dashed lines indicate contacts between traxels. Visible in these boxes is the gutter-like effect between the traxels.

Figure 6.3 (a) shows that decreasing the extrusion width does have an increasing effect on both the bending angle as well as the resistance. However, the effect on the bending angle is largely overshadowed by the standard deviations on the measurements. The microscopic views of the cross-sections of the sheets give some explanation of the smaller than expected effect on the bending angle. Figure 6.3 (b) shows that for an extrusion width of 0.4 mm the contacts appear to be taller than the rest of the material, resulting in ridges. Figure 6.3 (c) shows that for a sample with an extrusion width of 1.2 mm the contacts are shorter than the rest of the material, resulting in a gutter-like effect. The result of this is that the material appears to have contacts with a larger height for lower extrusion widths, which might negate the effect of having more contacts. To confirm whether changing the extrusion width setting caused over- or underextrusion, the samples were weighed. Neither the samples with a lower extrusion width nor those with a higher extrusion width compared to the default 0.6 mm showed any significant weight difference to the weight of the samples printed with the default parameters.

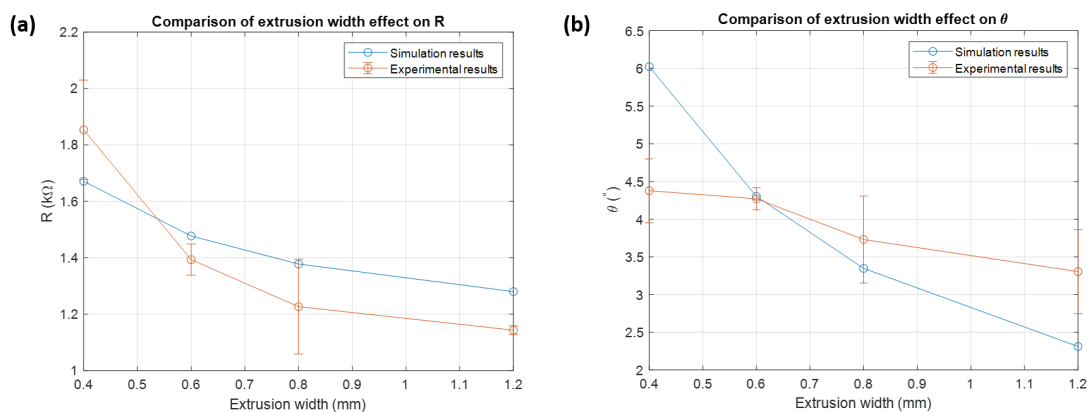


Figure 6.4: Comparison of the effect of extrusion width on the sample properties in the FEM model and experimental results. (a) Comparison of resistances. (b) Comparison of bending angles.

Figure 6.4 shows a comparison of the effect of the extrusion width between the FEM model and experimental results. Interestingly, the results for the resistance appear quite comparable and show similar dependencies on the extrusion width. However, the comparison for the bending angle shows that the bending angle in the experiments had a dissimilar dependence on the extrusion width. One explanation for this difference could be the earlier discussed ridges and gutters that can be seen in the cross-sectional images in Figure 6.3. However, this would not explain the steeper slope seen in the resistances of the samples.

6.6 Extrusion multiplier and infill density

As previously discussed in Section 3.4, the extrusion multiplier and infill density settings are thought to have similar effects on the properties observed in the sample. It is thought that extruding less material, meaning a lower multiplier or density, could cause less well formed contacts and thus an increase in the bending angle and resistance. The infill density cannot be changed above its default setting in Table 5.1, but the extrusion multiplier does offer this possibility. The effect of increasing the extrusion multiplier to overextrude filament was thought to have a positive effect on the forming the contacts and thus to decrease the bending angle and resistance.

Figure 6.5 (a) shows that the effect of changing the extrusion multiplier has highly varying results. Underextrusion of filament seems to increase the resistance, but has almost no significant effect on the bending angle. Printing the samples with an extrusion multiplier of 0.5 seemed to result in either samples with no visible contacts with a bending angle close to the

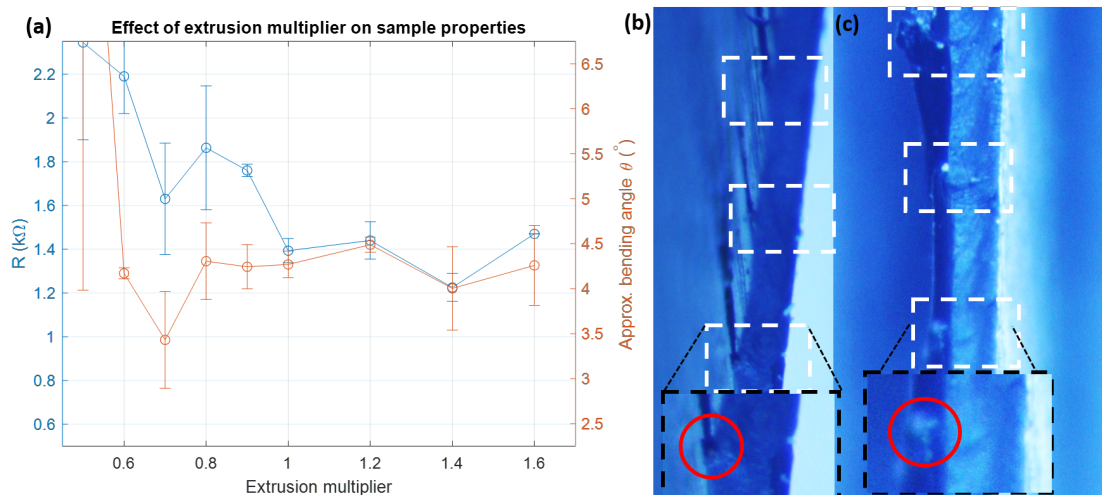


Figure 6.5: (a) Results of varying the extrusion multiplier with errorbars of length equal to the standard deviation. (b) Microscopic view of the cross section of a sample printed with a 1.0 extrusion multiplier. Boxes with white dashed lines indicate contacts between traxels. There are small gutters visible as darker lines perpendicular to the contact surface. The black dashed box shows a zoomed in gutter. (c) Microscopic view of the cross section of a sample printed with a 1.6 extrusion multiplier. Boxes with white dashed lines indicate contacts between traxels. The black dashed box shows a zoomed in contact, where the cross-section of a ridge is visible. The thickness has not visibly increased. Note: imagery of samples printed with extrusion multipliers lower than 1 is unavailable due to the samples breaking when removing them from the wafers.

maximum of 45° or samples with visible contacts that exhibited similar behaviour to those printed with a higher extrusion multiplier. Overextrusion of the filament also showed little effect. Figure 6.5 (b) shows that there are slight gutters between the traxels when printing with a 1.0 extrusion multiplier. The black box shows a slightly zoomed in image in which the gutter is more clearly shown. Figure 6.5 (c) shows ridges when printing with an extrusion multiplier of 1.6. However, this shows little effect on the resistance and bending angle in Figure 6.5 (a). Weighing the samples showed that the extrusion multiplier affected the weight of the samples. For example, a sample with an extrusion multiplier of 0.5 weighed 14 g, which is 46% less than the default samples. It is thought this is largely due to the effect of the extrusion multiplier on the thickness of the samples.

The infill density (see Section 3.4) was tried as an alternative to the extrusion multiplier in order to get more consistent results. Again, it was expected that a lower infill density would result in less material to fill the contacts and thus a higher contact resistance and bending angle. Figure 6.6 (a) shows that the infill density has an effect on the properties of the sample similar to that of the extrusion multiplier. The resistance increases significantly for a lower infill density, which is as expected. However, there is no significant effect on the bending angle up until the transition from an infill density of 65 % to 60 %. Similarly to what happened for an extrusion multiplier of 0.5, samples printed with a 60 % infill density were suddenly printed with no contacts, which caused the bending angle and resistance to increase dramatically. This is further highlighted by the microscopy images in Figure 6.6 (b) and (c), where it can clearly be seen that the 65 % infill density sample still has quite well-formed contacts while the 60 % infill density sample has no contacts between the traxels. It is unknown why this transition between the two states is so sudden.

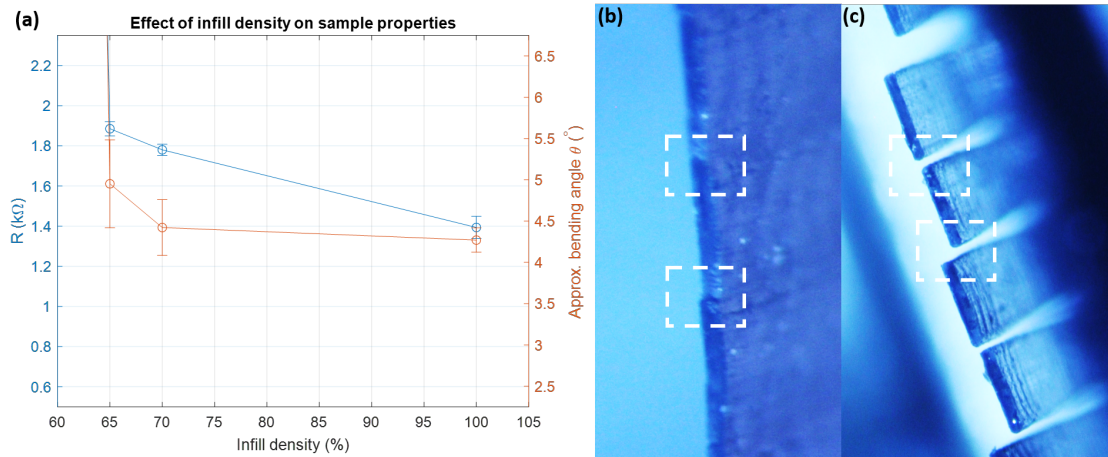


Figure 6.6: (a) Results of varying the infill density with errorbars of length equal to the standard deviation. (b) Microscopic view of the cross section of a sample printed with a 65 % infill density. Boxes with white dashed lines indicate contacts between traxels. (c) Microscopic view of the cross section of a sample printed with a 60 %. Boxes with white dashed lines indicate contacts between traxels.

6.7 Layer height

The effect of the layer height was discussed in Section 3.3.2 and modelled in Section 4.3.3. The expectation was that the layer height would have a large effect on the resistance of the sample, as a greater layer height would result in a greater cross-sectional area. Additionally, depending on whether the height of the contact area would grow along with the layer height, the bending angle could also be affected.

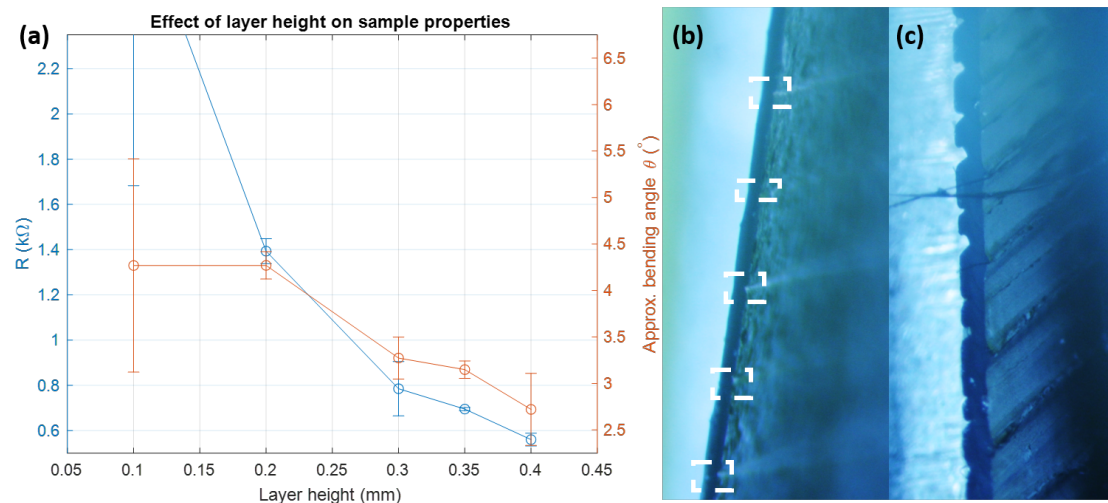


Figure 6.7: (a) Results of varying the layer height with errorbars of length equal to the standard deviation. (b) Microscopic view of cross-section of a sample printed with a layer height of 0.1 mm, the contacts are highlighted with boxes of white dashed lines. Note the even distance between contacts. (c) Microscopic view of cross-section of a sample printed with a layer height of 0.35 mm. The contacts are visible as strong gutters on the left side of the sample. Note how the contacts are unevenly spaced.

Figure 6.7 (a) shows that the effect of the layer height on the resistance is largely as expected. However, the effect on the bending angle is largely unexpected. For the lower layer height of 0.1 mm, the angle remains unaffected, which indicates that the contact heights scaled along with the layer height. However, for higher layer heights, the bending angle actually decreases,

where it was expected it would remain constant or increase. Figure 6.7 (b) shows that for a layer height of 0.1 mm the contacts are evenly spaced, which is as expected. However, Figure 6.7 (c) shows that for a layer height of 0.35 mm the contacts are highly unevenly spaced. This effect is further investigated in microscopic images taken of the top and bottom of the samples. Fig-

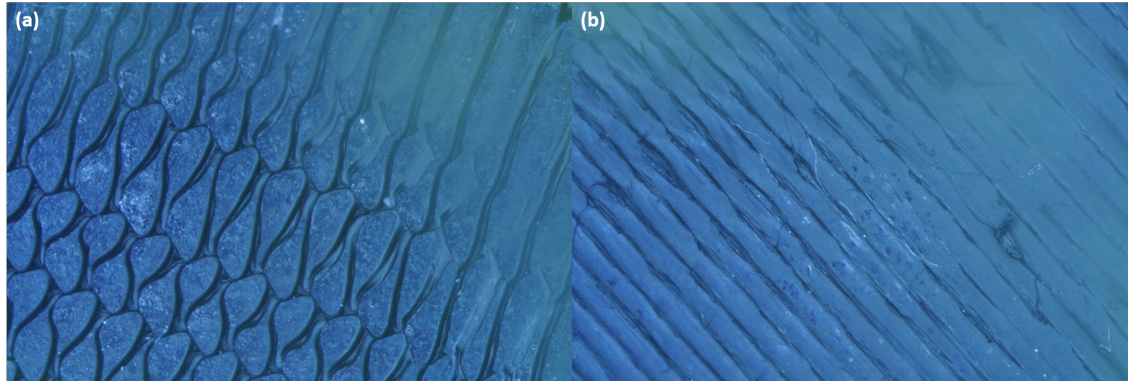


Figure 6.8: (a) Bottom of a sample printed with 0.35 mm layer height. (b) Top of the same sample at the same location.

ure 6.8 (a) shows that, in some areas, the bottom of a 0.35 mm layer height sample transitions from the usual traxel shape into an unusual wave-like pattern. Figure 6.8 (b) shows that the wave pattern is not visible from the top of the sample. It is thought that the wave pattern could be the cause for the unexpected decrease in bending angle in these samples. As previously mentioned in Section 3.3.2, it could be that the cause for this wave pattern is that the layer height is set too close to the nozzle diameter, which makes it difficult for the printer to keep the layer height steady.

The same phenomenon was observed in a sample with a 0.4 mm layer height, but not in the sample of 0.3 mm. This indicates that either this effect is not always visible on the outside of the sample, or that there is another cause for the bending angle decreasing. Weighing the samples showed that the layer height affected the weight of the samples. For example, a sample with a layer height of 0.4 mm weighed 0.53 g, which is 100 % more than the default samples (see Section 6.1).

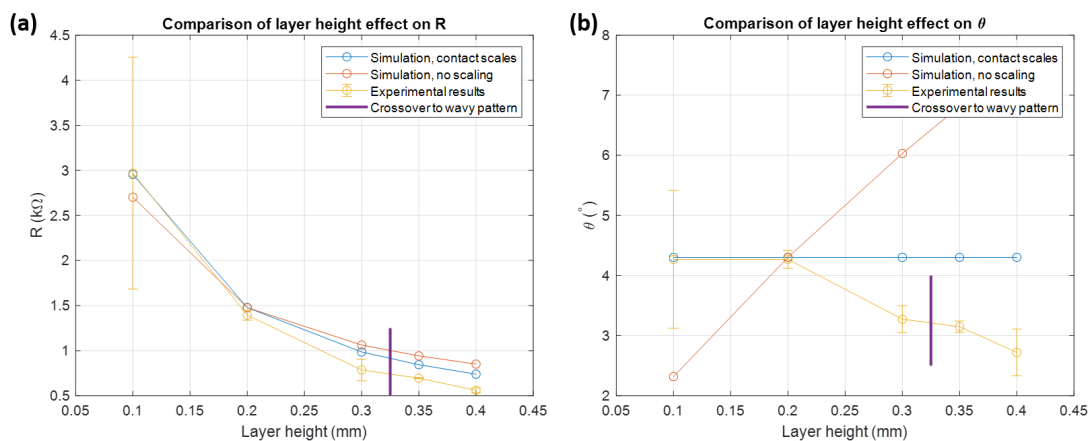


Figure 6.9: Comparison of the effect of the layer height on the sample properties in the model and experimental results. Purple lines indicate after which point the samples started exhibiting a 'wavy' pattern. (a) Comparison of resistances. (b) Comparison of bending angles.

Figure 6.9 (a) shows that the resistance of the sample behaves quite similarly to the FEM model. The FEM model results do fall outside of the experimental standard deviations, but it is thought this could be caused by the wavy pattern in Figure 6.8. Figure 6.9 (b) again indicates the large difference in effects, as the FEM model results are completely different from the experimental results.

6.8 Combined parameters

So far, only the effect of individually changing printing parameters has been studied. It is important to know whether these effects can be added together when combining different printing parameters. In this case, only the printing parameters with consistent effects were combined. These were the bed temperature, the nozzle temperature and the extrusion width.

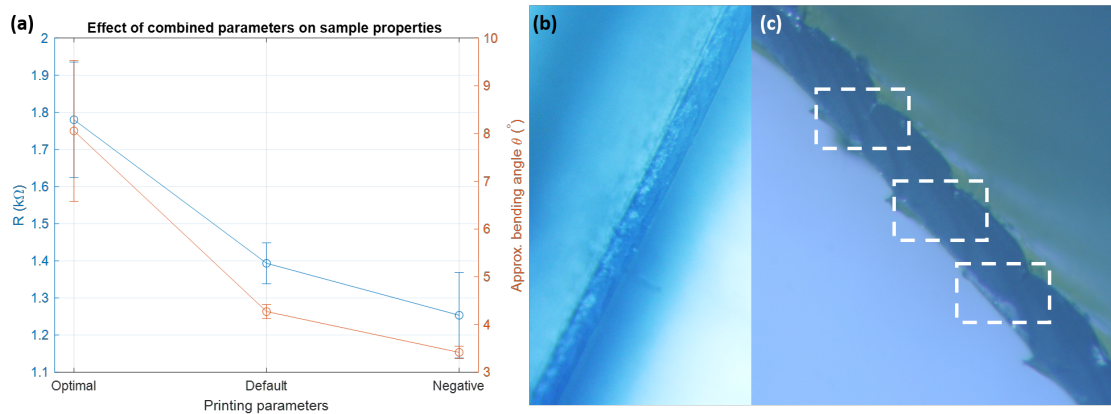


Figure 6.10: (a) Comparison between printing with bending angle optimized settings (25 °C bed temperature, 200 °C nozzle temperature, extrusion width 0.4 mm), default settings (Table 5.1), and settings that negatively affect the bending angle (70 °C bed temperature, 230 °C nozzle temperature, extrusion width 0.8 mm). (b) Microscopic image of the cross section of a sample printed with the printing parameters that have a negative effect on the bending angle. Note the lack of clearly defined contacts. (c) Microscopic image of a sample printed with the printing parameters that optimize the bending angle. The contacts are indicated by boxes of white dashed lines. Note that the contacts now have a gutter-like effect.

Figure 6.10 (a) shows that combining the parameters indeed combines their effect. The bending angle is increased by an average of 89 % compared to the default parameters when printing with the optimal parameters. When printing with the 'negative' parameters, it is decreased by an average of 20 %. These effects are supported by the microscopic images of the cross-sections. Figure 6.10 (b) shows that no contacts or gutters are visible for the 'negative' parameters. Figure 6.10 (c) shows that, instead of the visible contact lines between the traxels as was visible in Figure 6.1 and Figure 6.2, there are now visible gutters between the traxels. This is the opposite effect as was visible for the extrusion width of 0.4 mm in Figure 6.3, which showed visible ridges. It is thought the transition from ridges into gutters is caused by the change in the temperature settings, and that the gutters are the cause of the increased bending angle.

Figure 6.11 shows IR thermography images taken of the samples with combined printing parameters. Figure 6.11 (d) shows the expected heating pattern, namely that the diagonal from the top right to the bottom left heats up with the associated corners heating up the most. The difference between the IR thermography images is not very large. However, it is visible that the sample printed with the 'negative' printing parameters in Figure 6.11 (c) shows a much less concentrated heating of the sample around the diagonal than the sample in Figure 6.11 (a).

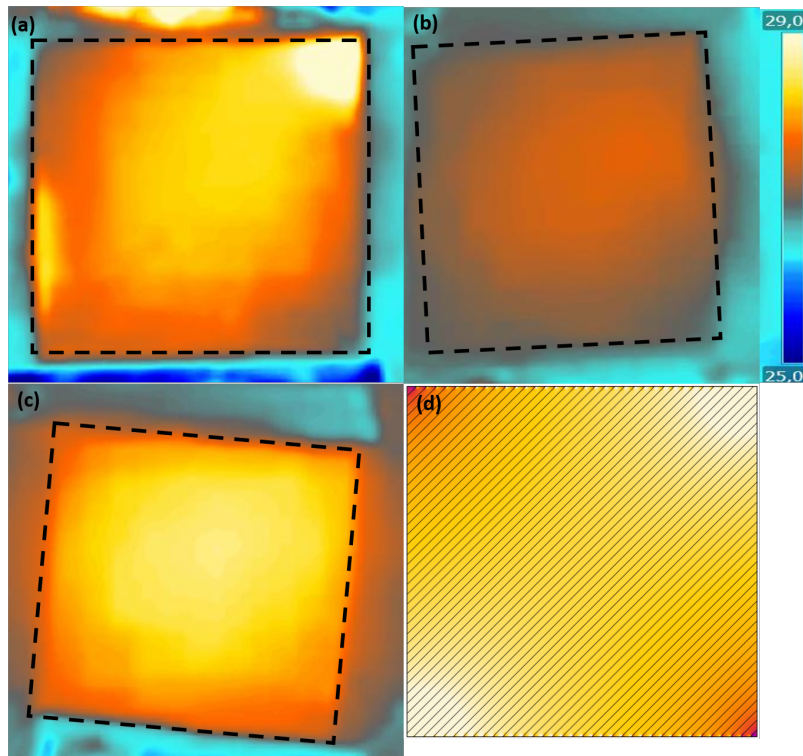


Figure 6.11: Heat signatures captured using IR thermography after samples are connected to a 30 V terminal voltage. Images are mapped on a 25 °C to 29 °C temperature range. Black striped borders indicate the location of the samples. **(a)** One of the samples printed with optimal parameters. **(b)** One of the samples printed with the default parameters next to the color scale for (a), (b) and (c). Note: this sample is considerably less hot, which is thought to have been caused by letting it heat up for less long than the other samples. **(c)** One of the samples printed with printing parameters minimizing the bending angle. **(d)** Plot of the natural logarithm of the electric energy density of the FEM model with default parameters, indicating the expected heating pattern.

6.9 Metamaterial application

One application of an anisotropically conductive metamaterial is that of a concentrator [6, 10, 49]. It is a sheet that concentrates current in its middle.

Figure 6.12 **(a)** shows a 3D-printed concentrator sheet. Figure 6.12 **(b)** shows a 3D-printed sheet with an infill printed fully perpendicularly to the terminals. Two concentrators were printed, one with the default parameters from Table 5.1 and another with optimal parameters as discussed in Section 6.8.

Figure 6.13 **(d)** indicates the expected heating pattern of the concentrators. Figure 6.13 **(a)** shows that the sheet printed perpendicularly to the terminals heats up uniformly. Figure 6.13 **(b)** shows that the concentrator with the default values indeed concentrates the current in its middle. This is evident from the fact the sheet heats more in the middle than the perpendicularly printed sheet. Figure 6.13 **(c)** shows that the optimal printing parameters increase this effect, as the heating of the sample is further restricted to the middle and corner points. The resistances of the samples show that the concentrator printed with the default parameters has a much higher resistance than the other concentrators. This is unexpected, as the resistance for the optimal parameters should be higher. It could be that there is some Ag-conductive paint between the sample and wafer in the upper left corner of Figure 6.13 **(c)**, where the sample heats up considerably less. This would then also cause a lower resistance.

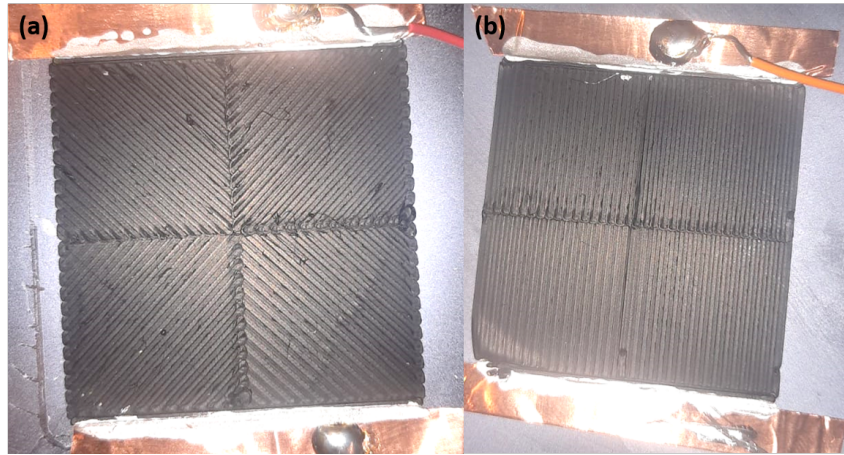


Figure 6.12: 40 mm by 40 mm 3D-printed sheets consisting of four smaller 20 mm by 20 mm sheets. **(a)** The sheets are at an angle to create a current-concentrating metamaterial. **(b)** The sheets are all perpendicular to the terminals.

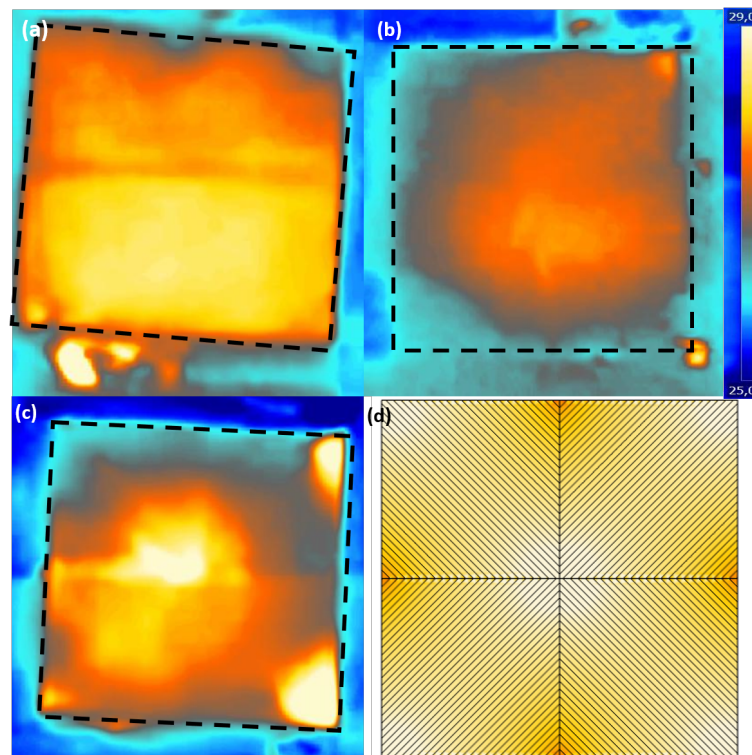


Figure 6.13: Heat signatures of the metamaterials shown in Figure 6.12. Images are mapped from black to white on a 25 °C to 29 °C temperature range. **(a)** Sheet printed fully perpendicular to the terminals. $R = 1.26 \text{ k}\Omega$ **(b)** Concentrator printed with default values from Table 5.1 next to the color scale for (a), (b) and (c). $R = 1.71 \text{ k}\Omega$. **(c)** Concentrator printed with bending angle optimizing parameters as used in Section 6.8. $R = 1.33 \text{ k}\Omega$. **(d)** The electric energy density of a concentrator modelled in FEM with default parameters, indicating the expected heating pattern.

6.10 Conclusions

This chapter shows the experimental results from characterizing the metamaterials. The default print settings produce a 4.27° bending angle. It is found that the extrusion width, bed temperature and nozzle temperature settings are able to consistently affect the anisotropic con-

duction in the metamaterials. By contrast, the layer height, extrusion multiplier and infill density are unable to do so, and in some cases show unreliable or unexpected results. Most of the results are explained through microscopy images of the cross-sections of the metamaterials. By combining the optimal settings for the extrusion width, bed temperature and nozzle temperature, the bending angle is raised to 8.05° . A demonstration of a current concentrating metamaterial is given and is shown to concentrate the flow of current through IR thermography. Using the optimal parameters on this concentrator results in an amplified effect.

7 Discussion and conclusion

This chapter discusses the results of the research presented in this report. The discussion gives a comparison of the expectations and results. The conclusion summarizes the report with the main conclusions. Finally, recommendations are given for future research.

7.1 Discussion

7.1.1 Fabrication

One consistency problem was the silicon wafers used as printing surfaces. All silicon wafers used in the process had previously been used for other research purposes. This meant that their origins were unknown, and some were treated with different materials. This mainly caused inconsistencies because some worked a lot better as printing surfaces than others. One solution to this could be to use untreated, new wafers. Another consistency problem was applying the Ag-conductive paint. Due to its low viscosity it easily flowed underneath the samples. This has a large effect on the conduction characteristics of the samples, as the silver paint is much more conductive than the printed filament. Hence, all these samples were disregarded.

The biggest influence on whether the print would stick seemed to be the bed temperature. Especially a bed temperature of 25 °C would often result in failed prints. Therefore, it is advised to maintain a bed temperature of at least 40 °C when printing on silicon wafers for consistent results.

7.1.2 Measurements

One of the biggest uncertainties in this research was the voltage probing method for finding the bending angle Section 4.4. The method is only based on the FEM simulation. As the found bending angles never exceeded past 8.05°, it is thought that the approximation was only ever used in the region of Figure 4.10 where the linear approximation was quite accurate. Further investigation of the method also showed that the linear interpolation was only accurate in the special case that the sample was square and the sample angle φ was 45°. In different cases, the bending angle and voltage difference showed a much more complex relation. The effect of meanders on this relation is briefly discussed in Appendix B.

The voltage measurement methodology could also have been affected because high voltages of 10 V, 20 V and 30 V were used. This could have warmed the material and affected its resistivity in certain areas. This was investigated by analyzing four random samples at 2 V, 5 V, and 10 V, which resulted in a 0.9 % lower average bending angle. This likely does not affect the validity of the measurements, as the voltage difference measurements typically have a standard deviation far larger than this decrease.

Conductive filament is known to fluctuate in resistance for at least a few days after being printed [50]. To study the magnitude of this effect, the resistance of three random samples was measured again 14 days after printing. The sample resistances had decreased an average of 5 %. This did not significantly affect the comparisons between the resistance of the samples, as all were measured within two hours of printing.

The images from IR thermography are highly influenced by factors such as reflection from the environment and the amount of time current had been flowing. Results could improve a lot if they were done in a controlled, reflectionless, environment, with a camera with a higher resolution, and above all if samples are photographed at exactly the same times. Printing on glass wafers could also have helped as they are less thermally conductive. A clearer heating pattern could be derived using lock-in thermography [9], a process by which a low-frequency AM driving voltage is used on the sample. The sample is filmed with the IR camera, and the resulting

data is band-pass filtered for the driving frequency. This clears out a lot of the thermal noise and disturbances from the surroundings.

The microscope images were often unclear. It is likely they could have benefited from better lighting conditions to further show the structure of the traxels. Another improvement could be taking Scanning Electron Microscope (SEM) images, as this would allow for close-ups around the contacts. An example of this can be found in Figure 2.2.

7.1.3 FEM Simulation

The FEM simulation uses a number of assumptions. One of these is that the meanders in the sample do not have a large effect on its conduction characteristics for low contact resistivities. A model with meanders is made in Appendix B. This model shows that the bending angle characteristics are almost exactly the same, but that the upper limit for the resistance is roughly half that of the model without meanders. It is thought this does not heavily affect the comparisons of the model with the experimental results as the found bending angles were relatively low. This problem could be solved by finding a way to print the samples without the meandering effect, or to consistently remove the meanders.

7.1.4 Experimental results

The **bed temperature and nozzle temperature** showed similar results. Microscopic images supported the expectation that they had an effect on the fusing of the traxels. One effect that both share is that, when they are above the manufacturer suggested settings, the resistance increases. This is unexpected, especially considering the bending angle does decrease, which indicates better contacts. One explanation could be that the higher temperature somehow equally affects the conductivity both in the traxels as well as in the contacts, perhaps through deteriorating the material. The effect of these temperatures on the resistivity of the material could be tested, for example by heating prints in the oven.

The **extrusion multiplier** was shown to have highly varying results. Increasing it showed no significant effects, while decreasing it only resulted in an increased resistance with the bending angle remaining constant. It is thought this is caused by the extrusion multiplier having an equal effect on the size of the contacts as well as the traxels, thereby causing no difference on the bending angle. However, this does not explain the lack of a decreased resistance for a higher extrusion multiplier. One explanation could be that overextrusion deteriorates the material in some way.

The results for the **infill density** were much more consistent but the mean behaviour seemed to be similar to that of the extrusion multiplier. It is thought this is caused by the printed traxels flowing together despite the intended distance between them being larger. This then results in traxels with a lower height and better filled contacts.

One effect the extrusion multiplier and infill density have in common is a small transition region after which contacts are no longer printed and the bending angle peaks to 45°. This transition region was too small to accurately use for influencing the contacts, which means neither setting is useful in manipulating the anisotropic conduction. Previous research also found a small transition region for whether traxels made contact or not [40].

The **extrusion width** did not show the strong results expected from the theory or simulations. This was partly explained by microscopy images that showed smaller traxel widths resulted in ridges in the contacts. However, it is unknown why the contacts are shaped differently depending on the extrusion width. It could be that the nozzle itself had an effect, as it is suggested to keep extrusion widths below the outer nozzle diameter [42] for good quality prints.

The effect of the **layer height** was likely affected by the wavy pattern that was shown in microscopic images. Samples with this pattern might have bigger contact areas between traxels,

which would cause a lower bending angle. As it is commonly suggested to use layer heights below 80 % of the nozzle diameter [42, 43], it is thought this pattern is printed because the nozzle does not press on the filament enough. It is thought that this pattern is related to rheology effects in the nozzle [51]. The same pattern was not found in a 0.30 mm sample, which already showed a decreased bending angle. This could be because the pattern was less obviously noticeable, or that there is some other effect which also decreases the bending angle.

7.1.5 Combined Parameters

The biggest problem with combining the extrusion width, bed temperature and nozzle temperature is that they also have large effects on the print quality and consistency. This means that prints with the parameters that are optimal for the bending angle often fail.

7.1.6 Metamaterial Applications

The metamaterial application example of a concentrator showed significant improvement when printed with the combined parameters that optimized the bending angle. A further improvement could be to use a custom infill pattern to allow the concentrators to be printed without meanders or overlap.

7.2 Conclusion

The conclusion summarizes the results of the research presented in this report by individually answering every subquestion as presented in Section 1.3. After this, the main research question is answered in a summarizing statement.

How does the previous knowledge from the thermal domain on steady state metamaterials translate to the electrical domain?

Most recent knowledge on steady state metamaterials is in the thermal domain and with metamaterials created by a layer-wise arrangement of two different materials that are able to bend heat flux. This knowledge can be translated to the electrical domain as static heat flow and static electric fields are both governed by the Laplace equation. Tarkhanyan et al. [30] provide a model of how a similar arrangement of two electrically conductive materials can be used to bend electric current. This model was then adapted to anisotropic conductivity as found in 3D-printed structures

How do the printing properties of a 3D-printed anisotropic conductive material affect its anisotropic properties?

A 3D-printed anisotropic conductive material has anisotropic conduction due to a having contact resistivity $\sigma_{(c)}$ between traxels with bulk resistivity ρ_c of finite thickness T_w . Together, these parameters affect the anisotropic conduction and thus the bending angle inside a 3D-printed metamaterial. This anisotropic conduction can be affected by the printing parameters used in the process of fabricating the metamaterial. Table 7.1 summarizes the results found for each printing parameter.

How can a 3D-printer be used to produce these properties and optimize them to achieve a maximal bending angle?

An FEM model was made that showed it should be possible to attain a bending angle using previously found values for 3D-printed sheets.

The anisotropic properties can be produced through use of slicing software to choose the infill pattern of a 3D-print. The materials can then be printed on silicon wafers, which allows them to be removed from the print bed without affecting them. Electrical connections to these metamaterials can be made using Ag-conductive paint.

The bending angle can be reliably optimized by lowering the bed temperature, nozzle temperature and extrusion width during the printing process. In this research, this resulted in an

Parameter	Direction	Effect
Bed Temperature	↑	R↑ θ ↓
	↓	R↑ θ ↑
Nozzle temperature	↑	R↑ θ ↓
	↓	R↑ θ ↑
Extrusion width	↑	R↑
	↓	R↓ θ ↓
Extrusion multiplier	↑	R↑
	↓	None
Infill density	↓	R↑
Layer height	↑	R↓ θ ↓
	↓	R↑

Table 7.1: Summary of the significant effects of the printing parameters that were tested. The **Direction** column indicates the direction in which the parameter was changed from the baseline value in Table 4.1.

average 89 % increase in the bending angle. Metamaterials printed with these parameters also showed significant effects compared to those printed with default printing parameters in IR thermography. However, these printing parameters also make the printing process more difficult and unreliable.

How can the anisotropic properties of 3D-printed, conductive metamaterials be used to manipulate the flow of current through these structures?

The anisotropic properties of 3D-printed, conductive metamaterials has been shown to be able to bend the flow of current through them. Furthermore, it has been shown that the extrusion width, bed temperature and nozzle temperature settings used during the printing process can be used to manipulate these anisotropic properties. A more complex metamaterial called a concentrator was constructed, which showed stronger anisotropic conduction when it was printed with optimal properties.

7.3 Recommendations

This section includes recommendations for future research into this topic.

- AC Properties: One big element of possible research on these metamaterials is their behaviour in an AC situation. The voids between the contacts are thought [27] to cause capacitive properties in the sample. It could prove interesting to investigate the AC properties of the metamaterials.
- Vertical printing: One of the most promising ways to increase the bending angle in the sample is to print vertically, as this weakens the contact surfaces and allows for more optimal geometries for the traxels. A short discussion and proof of feasibility of vertically printing metamaterials is given in Appendix D
- Ranges of printing parameters and usage of different parameters: A limiting factor in this research was the possible range for certain printing parameters. These ranges could be expanded with more experimental 3D-printing options. For example, the use of a 0.25 mm nozzle would allow for a much smaller extrusion width, which could increase the bending angle. Another option is the use of a cooled printing bed that would draw more heat from the sample, thereby lowering the effect of sintering. In addition, the effect of the layer fan and the ironing process were mentioned in Section 3.2, but they were never experimentally investigated.

- **Filaments:** Multiple conductive filaments are currently available on the market [3] and more might become commercially available soon. These filaments all have different bulk resistivities, but could also show very different contact behaviour depending on their viscosity. This gives a very broad range of filaments that could be tested, which might show much greater bending angles.
- **Alternating filaments** The related work in the thermal domain presented in Chapter 2 makes use of two different isotropic conductive materials that are arranged in an alternating pattern. Similar structures could be 3D-printed if a multi-material printer is used. As an example, the Protopasta conductive PLA filament [44] could be used alongside the carbon black-doped TPU filament used by Dijkshoorn et al. [9] The former was found in this research to have a bulk resistivity of $0.221 \Omega\text{m}$, while the latter was found to have a bulk resistivity of $2.8 \Omega\text{m}$. For a sample with equal thicknesses of both materials, the model by Tarkhanyan et al. [30] can be used and indicates they will have a $\theta = 32.8^\circ$ for a sample angle $\varphi = 45^\circ$. An adapted version of the FEM model from Chapter 4 indicates a $\theta = 31.2^\circ$. These are very strong results and thus they present a promising direction of research for 3D-printing metamaterials. Any contact resistances between either material could increase the bending characteristics even further. This method would also allow for more easy integration in other structures, as the anisotropic conduction would be much less dependent on the structure of the traxels and contacts. Additionally, it would allow for 3D metamaterial structures that are further shaped in the z -direction. It has been shown [39] that the properties of 3D-prints are different in higher layers than in the first layer of a material, as well as different in areas of the same layer, so this could prove for more consistent results.

In general, it appears that there is much potential in the field of printing anisotropic conductive metamaterials. By extending the range of the used parameters, stronger anisotropic conduction could be observed, but it is likely this direction of research is limited. A better outlook lies in vertical printing, which has been shown to have good potential for creation of strong anisotropic bending. An even greater potential can be found for printing with two or even more different conductive materials, as this would allow for greater and more easily fabricated metamaterials. This would then also greatly expand the amount of possible applications.

A Derivations of the analytical model

A.1 Derivation by Tarkhanyan et al.

Because the paper by Tarkhanyan et al. Tarkhanyan2017 skips a lot of steps in the derivation, an expanded version is described in this section. It should be noted with emphasis that the derivation in this section is entirely based on their work.

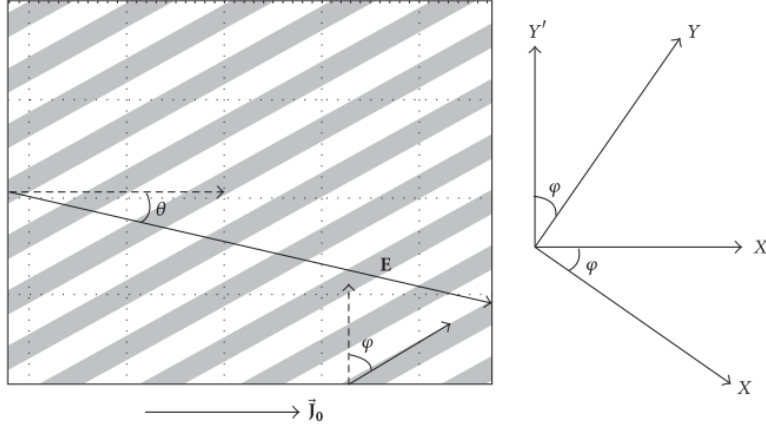


Figure A.1: The schematic used for the derivation by Tarkhanyan et al. [30], also shown in Chapter 2. A uniform current density \vec{J}_0 is applied to alternating layers of two materials with different isotropic conductivities at an angle φ . The resulting electric field \mathbf{E}' then is at a bending angle θ compared to the direction of the applied current density.

Figure A.1 shows a schematic of the situation described with their analytical model. The electric field vector can be described as

$$\mathbf{E} = \hat{\rho}_{\text{ef}} \mathbf{J} \quad (\text{A.1})$$

Where $\hat{\rho}_{\text{ef}}$ is the effective resistivity tensor and \mathbf{J} is the applied current density. In two dimensions, $\hat{\rho}_{\text{ef}}$ is:

$$\hat{\rho}_{\text{ef}} = \begin{bmatrix} \rho_{\text{xx}} & 0 \\ 0 & \rho_{\text{yy}} \end{bmatrix} \quad (\text{A.2})$$

Where:

$$\rho_{\text{xx}} = \frac{\rho_1 l_1 + \rho_2 l_2}{l_1 + l_2} \quad (\text{A.3})$$

$$\rho_{\text{yy}} = \frac{\rho_1 \rho_2 (l_1 + l_2)}{\rho_1 l_1 + \rho_2 l_2} \quad (\text{A.4})$$

are the homogenized resistivities in the x- and y-direction.

Note that here, it is already possible to derive β' for a situation with a ρ_b and σ_c , by taking

$$\rho_{\text{xx}} = \rho_b + \frac{\sigma_c}{T} \quad (\text{A.5})$$

which is the homogenized resistivity in the x-direction, and:

$$\rho_{\text{yy}} = \rho_b \quad (\text{A.6})$$

which is the homogenized resistivity in the y -direction. Using these resistivities will result in the same result as that found in Section A.2, where $\lim_{l_2 \rightarrow 0, l_2 \rho_2 = \sigma_c}$ is taken for the two-layered material.

To find the electric field in the x' , y' coordinate frame, $\hat{\rho}_{\text{ef}}$ has to be rotated by φ :

$$\hat{\rho}' = \hat{A} \hat{\rho}_{\text{ef}} \hat{A}^T \det |\hat{A}| \quad (\text{A.7})$$

Where \hat{A} is the rotation matrix

$$\hat{A} = \begin{bmatrix} \cos(\varphi) & -\sin(\varphi) \\ \sin(\varphi) & \cos(\varphi) \end{bmatrix} \quad (\text{A.8})$$

Note that the application of this matrix to $\hat{\rho}_{\text{ef}}$ is the same as that for κ , presented in Appendix C. The final result is that:

$$\hat{\rho}' = \begin{bmatrix} \rho_{\text{xx}} \cos^2(\varphi) + \rho_{\text{yy}} \sin^2(\varphi) & (\rho_{\text{yy}} - \rho_{\text{xx}}) \sin(\varphi) \cos(\varphi) \\ (\rho_{\text{yy}} - \rho_{\text{xx}}) \sin(\varphi) \cos(\varphi) & \rho_{\text{xx}} \cos^2(\varphi) + \rho_{\text{yy}} \sin^2(\varphi) \end{bmatrix} \quad (\text{A.9})$$

Thus, \mathbf{E}' can be found using $\mathbf{E}' = \hat{\rho}' \mathbf{J}_0$, as:

$$\mathbf{J}_0 = \begin{bmatrix} J_0 \\ 0 \end{bmatrix} \quad (\text{A.10})$$

$$\mathbf{E}' = J_0 \begin{bmatrix} \rho_{\text{xx}} \cos^2(\varphi) + \rho_{\text{yy}} \sin^2(\varphi) \\ (\rho_{\text{yy}} - \rho_{\text{xx}}) \sin(\varphi) \cos(\varphi) \end{bmatrix} \quad (\text{A.11})$$

Then, considering θ as the direction of \mathbf{E}' in the x' , y' coordinate frame:

$$\tan(\theta) = \frac{E_{y'}}{E_{x'}} = \frac{(\rho_{\text{yy}} - \rho_{\text{xx}}) \sin(\varphi) \cos(\varphi)}{\rho_{\text{xx}} \cos^2(\varphi) + \rho_{\text{yy}} \sin^2(\varphi)} \quad (\text{A.12})$$

Simplifying:

$$\tan(\theta) = \frac{(\rho_{\text{yy}} - \rho_{\text{xx}}) \tan(\varphi)}{\rho_{\text{xx}} + \rho_{\text{yy}} \tan^2(\varphi)} \quad (\text{A.13})$$

$$\tan(\theta) = \frac{(1 - \frac{\rho_{\text{xx}}}{\rho_{\text{yy}}}) \tan(\varphi)}{\frac{\rho_{\text{xx}}}{\rho_{\text{yy}}} + \tan^2(\varphi)} \quad (\text{A.14})$$

At which point β can be introduced and combined with Equation A.3 and Equation A.4:

$$\beta = \frac{\rho_{\text{xx}}}{\rho_{\text{yy}}} - 1 = \frac{l_1 \cdot l_2}{(l_1 + l_2)^2} \cdot \frac{(\rho_1 - \rho_2)^2}{\rho_1 \cdot \rho_2} \quad (\text{A.15})$$

Such that

$$\tan(\theta) = -\frac{\beta \tan(\varphi)}{1 + \beta + \tan^2(\varphi)} \quad (\text{A.16})$$

A.2 β for 3D-printed anisotropic materials

β can be rewritten to a system with a single resistivity $\rho_1 = \rho_b$ and a contact resistivity $l_2 \rho_2 = \sigma_c$ by taking the limit $\lim_{l_2 \rightarrow 0}$. This results in the adapted β' where $\beta' = \lim_{l_2 \rightarrow 0, l_2 \rho_2 = \sigma_c} \beta$. Note that in this case the resistivities are homogenized. Starting with the original equation for β :

$$\beta = \frac{l_1 \cdot l_2}{(l_1 + l_2)^2} \cdot \frac{(\rho_1 - \rho_2)^2}{\rho_1 \cdot \rho_2} \quad (\text{A.17})$$

Taking $l_1 = T_w$, $\rho_1 = \rho_b$, and applying $\rho_2 = \frac{\sigma_c}{l_2}$:

$$\beta' = \frac{T_w}{(T_w + l_2)^2} \cdot l_2 \cdot \frac{(\rho_b - \frac{\sigma_c}{l_2})^2}{\rho_b \cdot \frac{\sigma_c}{l_2}} \quad (\text{A.18})$$

Simplifying:

$$\beta' = \frac{T_w}{(T_w + l_2)^2} \cdot l_2 \cdot \frac{(\rho_b^2 - 2\rho_b \frac{\sigma_c}{l_2} + (\frac{\sigma_c}{l_2})^2)}{\rho_b \cdot \frac{\sigma_c}{l_2}} \quad (\text{A.19})$$

Further simplifying the right term:

$$\beta' = \frac{T_w}{(T_w + l_2)^2} \cdot \frac{(\rho_b^2 l_2^2 - 2\rho_b \sigma_c l_2 + \sigma_c^2)}{\rho_b \cdot \sigma_c} \quad (\text{A.20})$$

Taking $\lim_{l_2 \rightarrow 0}$:

$$\beta' = \frac{1}{T_w} \frac{\sigma_c}{\rho_b} \quad (\text{A.21})$$

A.3 Limits of θ for β

When taking the equation for θ as derived by Tarkhanyan et al. [30], it is interesting to investigate the behaviour of this equation depending on β'

$$\tan(\theta) = \frac{E_{y'}}{E_{x'}} = \frac{\beta' \cdot \tan(\varphi)}{1 + \beta' + \tan(\varphi)^2} \quad (\text{A.22})$$

Taking $\beta' \rightarrow 0$:

$$\lim_{\beta' \rightarrow 0} \theta = \arctan\left(\frac{0 \cdot \tan(\varphi)}{1 + 0 + \tan(\varphi)^2}\right) = 0 \quad (\text{A.23})$$

Taking $\beta' \rightarrow \infty$

$$\lim_{\beta' \rightarrow \infty} \theta = \arctan\left(\frac{\beta' \tan(\varphi)}{\beta'}\right) = \arctan(\tan(\varphi)) = \varphi \quad (\text{A.24})$$

A.4 Dependency of θ on φ

In this report, $\varphi = 45^\circ$ is consistently used, and the dependency of θ on φ is largely ignored. This is because the strength of the anisotropic conduction was seen as the main object of study. It is interesting, though, to shortly investigate this dependency and compare it between the analytical and FEM models. θ is known to have a maximum for a certain φ . This maximum can be found by differentiating Equation A.16 with respect to φ and setting the result to 0, then finding φ_{\max} . The online differential solver Wolfram Alpha was used to find:

$$\varphi_{\max} = \arctan(\sqrt{1 + \beta}) \quad (\text{A.25})$$

If this is used in Equation A.16 it gives:

$$|\theta|_{\max} = \arctan\left(\frac{\beta'}{2\sqrt{1 + \beta'}}\right) \quad (\text{A.26})$$

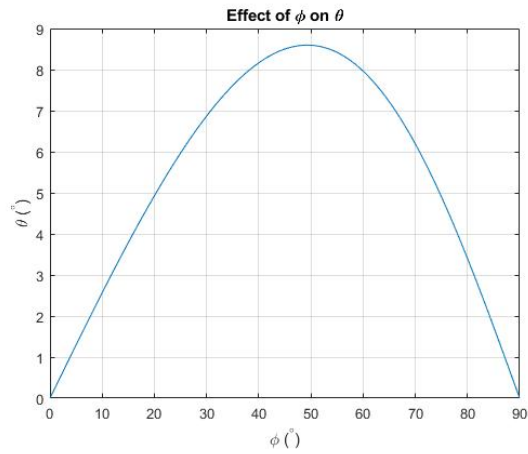


Figure A.2: The effect of φ on θ in the analytical model by Tarkhanyan et al.. The experimental parameters found in Chapter 6 are used.

For the found parameters in Table 6.1 this gives $\varphi_{\max} = 49.27^\circ$ and $\theta_{\max} = 8.90^\circ$.

Figure A.2 shows a comparison of the effect of varying φ . The limits for $\varphi = 0$ and $\varphi = \frac{\pi}{2}$ are both 0. This is logically explained, as fully vertically oriented traxels and fully horizontally oriented traxels both mean homogeneous conduction can take place between the two horizontally oriented terminals.

B Effect of meanders

The FEM model presented in Chapter 4 had straight traxels that have open ends outside of the material. However, as discussed in Chapter 5 the rectilinear infill pattern that is used for fabricating the sheets does feature a meander at the end of the traxels. As this meandering effect was not easily removed and it was thought not to have a large effect on the characteristics of the metamaterial for lower contact resistivities, it was left out. This appendix discusses an FEM model that does include meanders and how it affects the behaviour of the model.

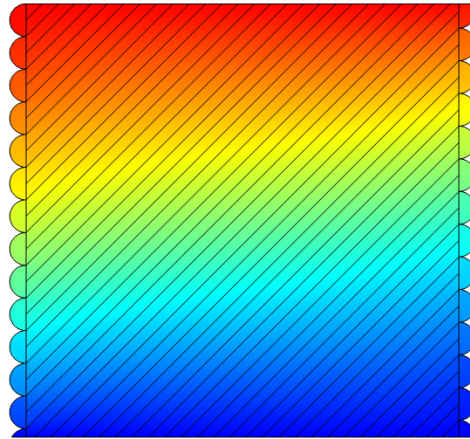


Figure B.1: Voltage potential in a FEM model that includes a meandering effect.

Figure B.1 shows the FEM model including the meandering effect. The used parameters are those from Table 4.1. The model shows a bending angle of 9.30° with a resistance of $21.5 \text{ k}\Omega$, these values are quite close (3.00 % increase in bending angle and 3.11 % decrease in resistance) to those discussed in Chapter 4.

Figure B.2 shows that the effect of the meanders is negligible in the lower contact resistivity range. In the higher contact resistivity range, the angle is also about the same, but the resistance radically differs. This is explained by observing the geometry in Figure B.1. It can be seen that, in the case of an extremely high contact resistivity, bulk conduction can now take place not just along the single traxel that connects to both terminals but also the traxel connected to it through a meander, thus causing the resistance in this case to be roughly halved. Furthermore, Figure B.2 (c) shows that the angle approximation through voltage probing presented in Section 4.4 actually fares better in the model with meanders, as the actual relation between the voltage difference and the bending angle is quite linear. It is thought this could have something to do with the different boundary conditions created by the meanders.

It should be noted that the model with meanders does not include the meandering effect at the sides of the terminals. This is because in the fabrication process the Ag-conductive paint is painted over these sections. It should also be noted that the actual meanders are printed diagonally as opposed to horizontally, as is the case in Figure B.1. However, it is thought this has little effect.

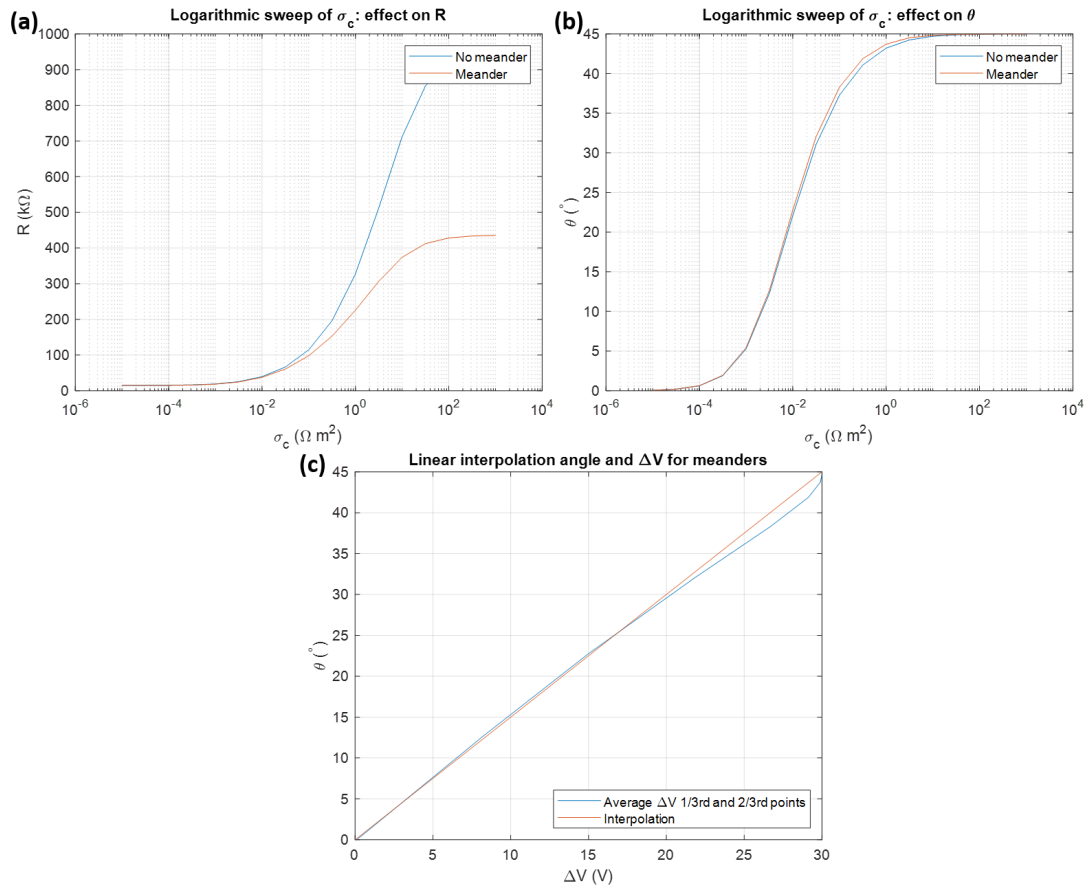


Figure B.2: Comparison of the effect of the contact resistivity in the sample for the model with and without meandering effect. **(a)** Effect on the resistance. **(b)** Effect on the bending angle. **(c)** The voltage difference at the 1/3rd and 2/3rd points (white dots in Figure 4.9) plotted together with the linear interpolation in Equation 4.3

C Modelling as anisotropic material

C.1 Conductivity tensor

If the conductivity across the samples is homogenized, the sample can be modelled as a single anisotropic material. This appendix shows how the conductivity tensor for the anisotropic material can be derived and modelled using FEM. Figure C.1 shows the vectors of the conductivity tensor in the directions parallel to and perpendicular to the traxels.

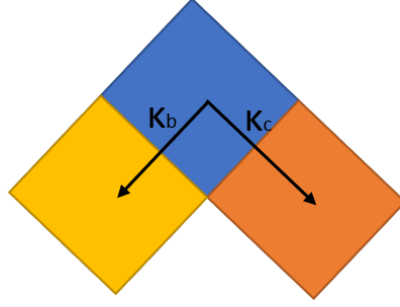


Figure C.1: Schematic of the conductivity tensor

In this case, the conductivity tensor in the coordinate frame rotated by φ is

$$\boldsymbol{\kappa} = \begin{bmatrix} \kappa_b & 0 \\ 0 & \kappa_c \end{bmatrix} \quad (\text{C.1})$$

The homogenized resistivity of the material in the direction perpendicular to the contacts ρ_c (across the contacts) is

$$\rho_c = \rho_b + \frac{\sigma_c}{T_w} \quad (\text{C.2})$$

For the conductivities, this holds that

$$\kappa_b = \frac{1}{\rho_b} \quad (\text{C.3})$$

$$\kappa_c = \frac{T_w}{\rho_b \cdot T_w + \sigma_c} \quad (\text{C.4})$$

This means the conductivity tensor in the frame of reference rotated by φ is known. In order to obtain the conductivity tensor in the Cartesian reference frame $\boldsymbol{\kappa}'$, this conductivity tensor has to be rotated by the rotation matrix $\mathbf{R}(\varphi)$:

$$\boldsymbol{\kappa}' = \mathbf{R}\boldsymbol{\kappa}\mathbf{R}^T \quad (\text{C.5})$$

Where:

$$\mathbf{R} = \begin{bmatrix} \cos(\varphi) & -\sin(\varphi) \\ \sin(\varphi) & \cos(\varphi) \end{bmatrix} \quad (\text{C.6})$$

This gives:

$$\boldsymbol{\kappa}' = \begin{bmatrix} \kappa_b \cos^2(\varphi) + \kappa_c \sin^2(\varphi) & \kappa_b \cos(\varphi) \sin(\varphi) - \kappa_c \sin(\varphi) \cos(\varphi) \\ \kappa_b \cos(\varphi) \sin(\varphi) - \kappa_c \sin(\varphi) \cos(\varphi) & \kappa_b \cos^2(\varphi) + \kappa_c \sin^2(\varphi) \end{bmatrix} \quad (\text{C.7})$$

If $\varphi = 45^\circ$ is used, this gives:

$$\boldsymbol{\kappa}' = \frac{1}{2} \begin{bmatrix} \kappa_b + \kappa_c & \kappa_b - \kappa_c \\ \kappa_b - \kappa_c & \kappa_b + \kappa_c \end{bmatrix} \quad (\text{C.8})$$

Filling in κ_b and κ_c gives:

$$\boldsymbol{\kappa}' = \frac{1}{2} \begin{bmatrix} \frac{1}{\rho_b} + \frac{T_w}{\rho_b \cdot T_w + \sigma_c} & \frac{1}{\rho_b} - \frac{T_w}{\rho_b \cdot T_w + \sigma_c} \\ \frac{1}{\rho_b} - \frac{T_w}{\rho_b \cdot T_w + \sigma_c} & \frac{1}{\rho_b} + \frac{T_w}{\rho_b \cdot T_w + \sigma_c} \end{bmatrix} \quad (\text{C.9})$$

C.2 COMSOL simulation

COMSOL can be used to simulate the metamaterial as a single anisotropically conductive material. In this case, the model values from Table 4.1 are used. Figure C.2 shows the potential field in the sample for these values.

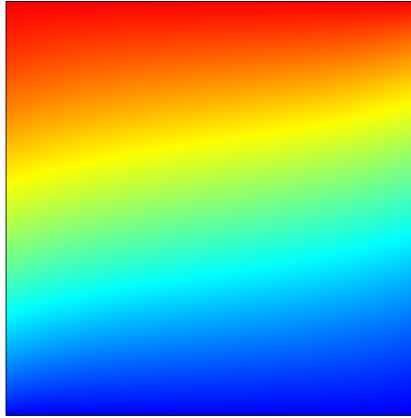


Figure C.2: Potential in the single anisotropic material

When the current density is used to determine the bending angle it is 9.00° , which is about the same as the 9.03° angle found in Chapter 4. However, as the contact resistivity in this situation is homogenized and the material has an anisotropic conductivity tensor, the electric field is not parallel to the current density. The angle of the electric field in the same point is -17.15° . If the same parameters are used in the homogenized model by Tarkhanyan et al. [30] presented in Equation 2.4 and Equation 2.6 it produces 17.2° . This interestingly shows the difference between the homogenized and non-homogenized FEM model (Chapter 4) as the current density stays the same but the electric field points in a different direction.

D Vertical printing

As mentioned in Chapter 4, the usage of the traxel width and layer height settings are limited through the nozzle diameter. For getting a higher bending angle, it is desired to decrease the width and increase the thickness of the traxels. The limit for either change is the nozzle diameter. One method to work around this limit is to print vertically. This flips around both printing parameters such that the extrusion width section now has the function of the traxel thickness and vice versa. In addition, it has been shown that 3D-objects printed vertically typically have lesser tensile strength [25, 31], which indicates lesser bonding between traxels and, in the case of conductive filament, might mean that the contact resistivity is increased. Another argument for vertical printing is that the traxels are not squished together against the printing bed.

However, there are downsides to printing vertically. It causes the contacts to be under the effect of gravity from different angles. These contacts are also closer to the heated bed. The combined effect could be that the traxels that are printed in the lower section might fuse better than those printed in higher sections, as they are pressed together by the higher layers. This could cause the contact resistivity to be lower in one side of the sample, which could skew results. In addition, slicing software does not allow for printing at an angle compared to the print bed, which means the sample would need to be printed parallel to the print bed, with the right shape having to be cut from it. This combination means vertical printing will likely require a more complicated fabrication process.

D.1 Experimental test

A vertical sample was prepared through printing a 30 mm by 30 mm square vertically using horizontal lines. The extrusion width was set to 1.2 mm while the layer height was set to 0.2 mm. The other printing parameters were the same as those in Table 5.1. A 45° sample was then prepared by cutting out a diamond shape using scissors. This diamond shape also had small extensions on two opposing surfaces, which would function as halfway probing points. Electrical contacts to the vertical sample also consisted of copper tape, but the adhesion consisted of both the Ag-conductive paint as well as a conductive epoxy. The resulting sample can be seen in Figure D.1.

As can be seen, the combined adhesive was not applied very well. This was because of the lack of flow-blocking lines like those present in the samples used for the study. Additionally, the lines indicating the probing points were quite thick and they seem misaligned. This significantly influences the accuracy of the measurement. Even so, the sample, which had a resistance of 197 k Ω , had an average homogenized voltage difference of 0.296. This indicates a bending angle of 13.32° according to the approximation presented in Section 4.4. This is quite a promising result and indicates possibilities for stronger bending angles with further manipulation of the printing parameters.

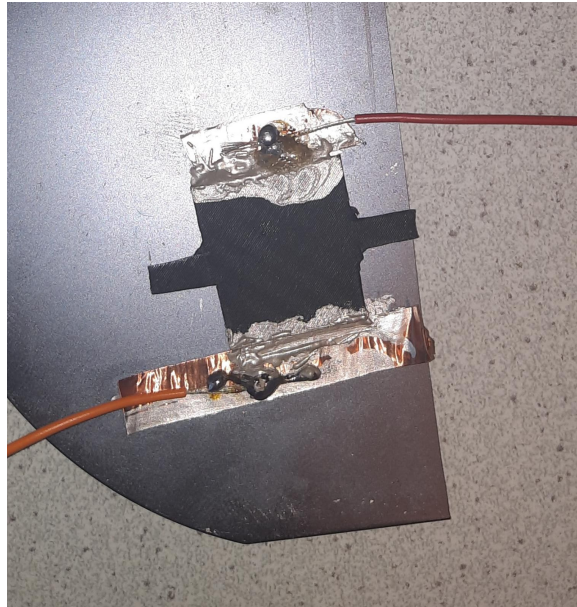


Figure D.1: Photograph of the vertically printed sample

E Failed fabrication methods

This appendix discusses some of the tried methods for parts of the fabrication process.

E.1 Printing surface

As previously mentioned in Chapter 5, the samples were printed on silicon wafers. This is far from an ideal print surface: the printed material does not stick well to the surface. This was largely remedied by heavy use of 3D-lac, but it was still hard to print on them with the sub-optimal print settings. Other print surfaces that were tested but went unused are presented in Table E.1

Print Surface	Problem
Hard paper	Paper warped after cooling down due to different heat expansion compared to printed material
Overhead sheets	Same problems as paper
Kapton tape on silicon wafers	Tape came loose too easily.

Table E.1: Unused print surfaces

E.2 Electrical Contacts

In Chapter 5 it is stated that Ag-conductive paint was a necessity for making electrical contacts due to its low viscosity. However, this viscosity also induces problems. Mainly, it allows the silver paint to flow into the voids between traxels and around the sample, which renders the sample skewed. In the case the connection between the sample and the wafer is not tight enough, the paint can also flow underneath the sample. A short summary of alternatives that were tried is given in Table E.2.

Method	Failure reason
Conductive Epoxy	Viscosity too high to make good contacts
Soldering tin	Barely made contact at all
Printing on copper tape	Filament does not stick to copper tape; Using 3D-lac makes the connection unconductive

Table E.2: Failed methods of creating electrical contacts

F Measurements per parameter

This appendix indicates the amount of samples that were tested to determine the effect of each printing parameter. The reason for including this information is that there were different amounts of samples tested for each datapoint, which causes a difference in the meaning of the standard deviation for the results presented in Chapter 6. It should be noted that 3 samples were intended to be printed per setting of a printing parameter, but that the actual amount of samples tested was sometime decreased to 2 samples due to a multitude of reasons. These reasons include difficulties printing samples, samples that got Ag-conductive paint spilled on them, and samples that were accidentally printed on wafers with a conductive layer. The total number of included samples is 64.

Extrusion multiplier	1.6	1.4	1.2	1	0.9	0.8	0.7	0.6	0.5
Amount	2	2	2	3	2	3	2	2	2
Layer Height (mm)	0.4	0.35	0.3	0.2	0.1				
Amount	2	2	2	3	2				
Ex. Width (mm)	1.2	0.8	0.6	0.4					
Amount	3	3	3	3					
Infill Density (%)	100	70	65	60					
Amount	3	2	2	2					
Bed Temp. (°C)	70	50	40	25					
Amount	3	3	2	2					
Noz temp. (°C)	230	215	206	200					
Amount	3	3	2	3					
Combined settings	Optimal	Default	Negative						
Amount	3	3	3						

Table F.1: The amount of samples that were printed, tested and included in the results per datapoint.

Bibliography

- [1] A. Babbar, V. Jain, D. Gupta, S. Singh, C. Prakash, and C. Pruncu, *Biomaterials and Fabrication Methods of Scaffolds for Tissue Engineering Applications*. 2020.
- [2] Y. Xu, X. Wu, X. Guo, B. Kong, M. Zhang, X. Qian, S. Mi, and W. Sun, *The Boom in 3D-Printed Sensor Technology*, vol. 17. 2017.
- [3] M. Schouten, G. Wolterink, A. Dijkshoorn, D. Kosmas, S. Stramigioli, and G. Krijnen, "A review of extrusion-based 3d printing for the fabrication of electro- and biomechanical sensors," *IEEE Sensors Journal*, pp. 1–1, 2020.
- [4] A. Dijkshoorn, P. Werkman, M. Welleweerd, G. Wolterink, B. Eijking, J. Delamare, R. Sanders, and G. J. Krijnen, "Embedded sensing: Integrating sensors in 3-D printed structures," *Journal of Sensors and Sensor Systems*, vol. 7, no. 1, pp. 169–181, 2018.
- [5] M. Askari, D. A. Hutchins, P. J. Thomas, L. Astolfi, R. L. Watson, M. Abdi, M. Ricci, S. Laureti, L. Nie, S. Freear, R. Wildman, C. Tuck, M. Clarke, E. Woods, and A. T. Clare, "Additive manufacturing of metamaterials: A review," *Additive Manufacturing*, vol. 36, no. September, p. 101562, 2020.
- [6] G. Park, S. Kang, H. Lee, and W. Choi, "Tunable multifunctional thermal metamaterials: Manipulation of local heat flux via assembly of unit-cell thermal shifters," *Scientific Reports*, vol. 7, no. September 2016, pp. 1–15, 2017.
- [7] A. Elkholy, M. Rouby, and R. Kempers, "Characterization of the anisotropic thermal conductivity of additively manufactured components by fused filament fabrication," *Progress in Additive Manufacturing*, vol. 4, no. 4, pp. 497–515, 2019.
- [8] J. F. Rodríguez, J. P. Thomas, and J. E. Renaud, "Mechanical behavior of acrylonitrile butadiene styrene fused deposition materials modeling," *Rapid Prototyping Journal*, vol. 9, no. 4, pp. 219–230, 2003.
- [9] A. Dijkshoorn, M. Schouten, G. Wolterink, R. Sanders, S. Stramigioli, and G. Krijnen, "Characterizing the electrical properties of anisotropic, 3d-printed conductive sheets for sensor applications," *IEEE Sensors Journal*, vol. 20, no. 23, pp. 14218–14227, 2020.
- [10] P. R. Bandaru, K. P. Vemuri, F. M. Canbazoglu, and R. S. Kapadia, "Layered thermal metamaterials for the directing and harvesting of conductive heat," *AIP Advances*, vol. 5, no. 5, 2015.
- [11] T. Han and C. W. Qiu, "Transformation Laplacian metamaterials: Recent advances in manipulating thermal and dc fields," *Journal of Optics (United Kingdom)*, vol. 18, no. 4, p. 0, 2016.
- [12] M. Maurizi, J. Slavič, F. Cianetti, M. Jerman, J. Valentinčič, A. Lebar, and M. Boltežar, "Dynamic measurements using fdm 3d-printed embedded strain sensors," *Sensors*, vol. 19, no. 12, 2019.
- [13] E. Fornells, E. Murray, S. Waheed, A. Morrin, D. Diamond, B. Paull, and M. Breadmore, "Integrated 3d printed heaters for microfluidic applications: Ammonium analysis within environmental water," *Analytica Chimica Acta*, vol. 1098, pp. 94–101, 2020.

- [14] K. Chizari, M. Arjmand, Z. Liu, U. Sundararaj, and D. Therriault, "Three-dimensional printing of highly conductive polymer nanocomposites for emi shielding applications," *Materials Today Communications*, vol. 11, pp. 112–118, 2017.
- [15] S. W. Kwok, K. H. H. Goh, Z. D. Tan, S. T. M. Tan, W. W. Tjiu, J. Y. Soh, Z. J. G. Ng, Y. Z. Chan, H. K. Hui, and K. E. J. Goh, "Electrically conductive filament for 3d-printed circuits and sensors," *Applied Materials Today*, vol. 9, pp. 167–175, 2017.
- [16] Y. Pang, Y. Cao, Y. Chu, M. Liu, K. Snyder, D. MacKenzie, and C. Cao, "Additive manufacturing of batteries," *Advanced Functional Materials*, vol. 30, no. 1, p. 1906244, 2020.
- [17] P. F. Flowers, C. Reyes, S. Ye, M. J. Kim, and B. J. Wiley, "3d printing electronic components and circuits with conductive thermoplastic filament," *Additive Manufacturing*, vol. 18, pp. 156–163, 2017.
- [18] H. K. Surmen, F. Ortes, and Y. Z. Arslan, *Fundamentals of 3D Printing and Its Applications in Biomedical Engineering*, pp. 23–41. Singapore: Springer Singapore, 2020.
- [19] I. Gibson, D. Rosen, and B. Stucker, "Additive manufacturing technologies: 3D printing, rapid prototyping, and direct digital manufacturing, second edition," *Additive Manufacturing Technologies: 3D Printing, Rapid Prototyping, and Direct Digital Manufacturing, Second Edition*, pp. 1–498, 2015.
- [20] J. Prusa, *Basics of 3D Printing*. 2019.
- [21] A. H. Espera, J. R. C. Dizon, Q. Chen, and R. C. Advincula, "3D-printing and advanced manufacturing for electronics," *Progress in Additive Manufacturing*, vol. 4, no. 3, pp. 245–267, 2019.
- [22] T. B. Palmić, J. Slavič, and M. Boltežar, "Process parameters for fff 3d-printed conductors for applications in sensors," *Sensors (Switzerland)*, vol. 20, no. 16, pp. 1–21, 2020.
- [23] Wikipedia, "Anisotropy - wikipedia." <https://en.wikipedia.org/wiki/Anisotropy> [Online; accessed 21-March-2021].
- [24] H. R. Wenk and P. Van Houtte, "Texture and anisotropy," *Reports on Progress in Physics*, vol. 67, no. 8, pp. 1367–1428, 2004.
- [25] E. Cuan-Urquizo, E. Barocio, V. Tejada-Ortigoza, R. B. Pipes, C. A. Rodriguez, and A. Roman-Flores, "Characterization of the mechanical properties of FFF structures and materials: A review on the experimental, computational and theoretical approaches," *Materials*, vol. 16, no. 6, 2019.
- [26] S. Garzon-Hernandez, D. Garcia-Gonzalez, A. Jérusalem, and A. Arias, "Design of FDM 3D printed polymers: An experimental-modelling methodology for the prediction of mechanical properties," *Materials and Design*, vol. 188, p. 108414, 2020.
- [27] A. Dijkshoorn and M. Schouten, "Modelling of Anisotropic Electrical Conduction in Layered Structures 3D-Printed with Fused Deposition Modelling [YET TO BE PUBLISHED]," pp. 1–36, 2021.
- [28] J. Zhang, B. Yang, F. Fu, F. You, X. Dong, and M. Dai, "Resistivity and its anisotropy characterization of 3D-printed acrylonitrile butadiene styrene copolymer (ABS)/carbon black (CB) composites," *Applied Sciences (Switzerland)*, vol. 7, no. 1, 2017.
- [29] B. Hampel, S. Monshausen, and M. Schilling, "Properties and applications of electrically conductive thermoplastics for additive manufacturing of sensors," *Technisches Messen*, vol. 84, no. 9, pp. 593–599, 2017.

- [30] R. H. Tarkhanyan and D. G. Niarchos, "Geometrically Tunable Transverse Electric Field in Multilayered Structures," *Advances in Condensed Matter Physics*, vol. 2017, 2017.
- [31] X. Gao, S. Qi, X. Kuang, Y. Su, J. Li, and D. Wang, "Fused filament fabrication of polymer materials: A review of interlayer bond," *Additive Manufacturing*, vol. 37, no. 2, p. 101658, 2021.
- [32] C. Bellehumeur, L. Li, Q. Sun, and P. Gu, "Modeling of bond formation between polymer filaments in the fused deposition modeling process," *Journal of Manufacturing Processes*, vol. 6, no. 2, pp. 170–178, 2004.
- [33] E. Sirjani, P. J. Cragg, and M. K. Dymond, "Glass transition temperatures, melting temperatures, water contact angles and dimensional precision of simple fused deposition model 3D prints and 3D printed channels constructed from a range of commercially available filaments," *Chemical Data Collections*, vol. 22, p. 100244, 2019.
- [34] L. Chaunier, G. D. Valle, D. Lourdin, A.-L. Réguerre, K. Cochet, and E. Leroy, "Viscous sintering kinetics of biopolymer filaments extruded for 3d printing," *Polymer Testing*, vol. 77, p. 105873, 2019.
- [35] M. Sardinha, C. M. Vicente, N. Frutuoso, M. Leite, R. Ribeiro, and L. Reis, "Effect of the ironing process on ABS parts produced by FDM," *Material Design & Processing Communications*, no. January 2020, pp. 1–7, 2020.
- [36] ALL3DP, "3d printer fan - do i really need one?." <https://all3dp.com/2/3d-printer-fans-do-i-really-need-one/> [Online; accessed 04-April-2021].
- [37] filament2print, "The importance of the layer fan." https://filament2print.com/gb/blog/76_importance-layer-fan.html [Online; accessed 04-April-2021].
- [38] G. Stano, A. Di Nisio, A. M. Lanzolla, M. Ragolia, and G. Percoco, "Fused filament fabrication of commercial conductive filaments: experimental study on the process parameters aimed at the minimization, repeatability and thermal characterization of electrical resistance," *International Journal of Advanced Manufacturing Technology*, vol. 111, no. 9-10, pp. 2971–2986, 2020.
- [39] S. A. Tronvoll, N. P. Vedvik, C. W. Elverum, and T. Welo, "A new method for assessing anisotropy in fused deposition modeled parts using computed tomography data," *International Journal of Advanced Manufacturing Technology*, vol. 105, no. 1-4, pp. 47–65, 2019.
- [40] S. Mousavi, D. Howard, F. Zhang, J. Leng, and C. H. Wang, "Direct 3D Printing of Highly Anisotropic, Flexible, Constriction-Resistive Sensors for Multidirectional Proprioception in Soft Robots," *ACS Applied Materials and Interfaces*, vol. 12, no. 13, pp. 15631–15643, 2020.
- [41] filament2print, "Wikipedia - mesoscale manufacturing." https://en.wikipedia.org/wiki/Mesoscale_manufacturing [Online; accessed 04-April-2021].
- [42] P. Carrier, "3d print speed: How to find the optimal speed for reliable and constant print quality." <https://dyzedesign.com/2018/07/3d-print-speed-calculation-find-optimal-speed/>, Jul 2018.
- [43] B. George, "Nozzle sizes - bob's project notebook documentation." https://projects.ttlxceeded.com/3dprinting_nozzle_sizes.html, Apr 2020.
- [44] Protoplant, "Proto-pasta conductive pla." <https://www.proto-pasta.com/pages/conductive-pla> [Online; accessed 21-March-2021].

- [45] M. Vinyas, S. J. Athul, D. Harursampath, and T. Nguyen Thoi, "Experimental evaluation of the mechanical and thermal properties of 3D printed PLA and its composites," *Materials Research Express*, vol. 6, no. 11, 2019.
- [46] Electrolube, "Electrolube silver conductive paint." <https://electrolube.com/product/scpsilver-conductive-paint/> [Online; accessed 21-March-2021].
- [47] T. Yang, X. Bai, D. Gao, L. Wu, B. Li, J. T. L. Thong, and C.-W. Qiu, "Invisible sensors: Simultaneous sensing and camouflaging in multiphysical fields," *Advanced Materials*, vol. 27, no. 47, pp. 7752–7758, 2015.
- [48] OHAUS, "Ohaus - scout pro." <https://us.ohaus.com/en-US/Products/Balances-Scales/Portable-Balances/Scout-Pro/Electronic-Balance-SP202-AM> [Online; accessed 07-April-2021].
- [49] W. X. Jiang, C. Y. Luo, H. F. Ma, Z. L. Mei, and T. J. Cui, "Enhancement of current density by dc electric concentrator," *Scientific Reports*, vol. 2, pp. 1–6, 2012.
- [50] D. Kosmas, "Model-Based Hysteresis Compensation and Control with 3D Printed Lousy Sensors [YET TO BE PUBLISHED]," 2020.
- [51] A. Das, E. L. Gilmer, S. Biria, and M. J. Bortner, "Importance of Polymer Rheology on Material Extrusion Additive Manufacturing: Correlating Process Physics to Print Properties," *ACS Applied Polymer Materials*, 2021.